PETROLOGICAL CONSTRAINTS ON THE ORIGIN OF PYROXENITE DYKES IN THE LITHOSPHERIC MANTLE OF THE CHESHMEH-BID OPHIOLITIC MASSIF, SOUTHERN IRAN

Alireza Eslami*,✉, Giulio Borghini, Alessandra Montanini***, Giovanni Grieco**** and **Claudio Marchesi°,°°**

* *ISTerre, Univ. Grenoble Alpes, Univ. Savoie Mont Blanc, CNRS, IRD, IFSTTAR, Grenoble, France.*
** *Dipartimento di Scienze della Terra, Università degli Studi di Milano, Italy.*
*** *Department of Chemistry, Life Sciences and Environmental Sustainability University of Parma, Italy.*
° *Departamento de Mineralogía y Petrología, Universidad de Granada, Spain.*
°° *Instituto Andaluz de Ciencias de la Tierra, CSIC-Universidad de Granada, Spain.*
✉ *Corresponding author, e-mail: alireza.eslami@univ-grenoble-alpes.fr*

Keywords: *hydrous boninite melt; supra-subduction setting; orthopyroxenite; Cheshmeh-Bid ophiolite massif; Iran.*

ABSTRACT

The Cheshmeh-Bid ophiolitic massif in the Khajeh-Jamali district (Southern Iran) is dominated by harzburgite-dunite tectonites locally intruded by orthopyroxenite dikes. These latter are composed of dominant coarse orthopyroxene with minor olivine, Cr-spinel, clinopyroxene and amphibole. Estimated equilibrium temperatures for Mg-hornblende and edenitic amphibole reveal a late stage magmatic origin.

The Cheshmeh-Bid orthopyroxenites are characterized by very low Al_2O_3, CaO, Na_2O and TiO_2 abundances coupled to relatively high MgO and SiO_2 contents. They display U-shaped REE patterns, selective LILE enrichment and positive Pb and Sr anomalies. The host harzburgites are highly refractory mantle residues resulting from fluid-assisted melting. Field observations and mineral assemblages suggest that the pyroxenites formed by melt injection along fractures within rather cold ambient harzburgites and chromitites at moderate pressure (P > 1 GPa). Based on bulk-rock compositions and mineral chemistry, we infer that the Cheshmeh-Bid orthopyroxenites originated from the intrusion and crystallization of hydrous Si-rich, low-Ca melts with a boninite signature in a supra-subduction environment. Fine-grained neoblastic domains developed in the pyroxenites in response to subsolidus ductile deformation and recrystallization, which were most likely related to the exhumation of the Cheshmeh-Bid ophiolite massif.

INTRODUCTION

Pyroxenite veins or layers are important constituents of the upper mantle and are diffusely distributed in ophiolitic and orogenic ultramafic massifs (e.g., Downes, 2007; Borghini et al., 2013; 2016; Bodinier and Godard, 2014), as well as mantle xenoliths (e.g., Gonzaga et al., 2010). Several hypotheses have been put forward to explain the origin of pyroxenites in mantle sections: (i) phase segregation within magmatic conduits in the mantle (e.g., Griffin et al., 1984; Bodinier et al., 1987; Python and Ceuleneer, 2003); (ii) recycling of subducted oceanic crust through mantle convection (e.g., Allègre and Turcotte, 1986; Kornprobst et al., 1990); (iii) interaction between ambient peridotite and pervasive infiltrating melts (e.g. Bodinier and Godard, 2003; Downes, 2007; Garrido et al., 2007; Borghini et al., 2016). During the last decade, formation mechanism of pyroxenites in peridotitic massifs has attracted attention mostly because they may represent proxies of mantle heterogeneities and provide insights on mantle processes such as partial melting, melt-rock interaction, melt migration and evolution through the upper mantle (e.g., Parkinson and Pearce, 1998; Godard et al., 2000; Kogiso et al., 2004; Montanini et al., 2006; 2012; Bodinier et al., 2008; Lambart et al., 2009; 2013; 2016; Gysi et al., 2011; Saccani et al., 2011; Borghini et al., 2013; 2016; 2020; Montanini and Tribuzio, 2015). Pyroxenite dykes/veins and layers ranging in composition from websterite to clino- and ortho-pyroxenite are commonly observed in the mantle section of supra-subduction zone ophiolites (e.g., Varfalvy et al., 1997; Tamura and Arai, 2006; Berly et al., 2006; Bodinier and Godard, 2014; Rogkala et al., 2017; Le Roux and Liang, 2019). Petrogenesis of these pyroxenites provides important constraints on the chemistry of the melts percolating in the supra-subduction environments.

This research focuses on the pyroxenite dykes and dykelets crosscutting the Cheshmeh-Bid peridotite massif in the Khajeh-Jamali ophiolitic massifs, Southern Iran (Fig. 1a, b). Previous works on harzburgite, dunite and podiform chromitite deposits of this ultramafic massif have revealed that mantle peridotites interacted with boninitic melts migrating through the supra-subduction mantle in a fore-arc setting (e.g., Rajabzadeh and Nazari Dehkordi, 2013; Shafaii Moghadam et al., 2014; Eslami et al., 2015; Monsef et al., 2018). However, the origin and petrologic significance of pyroxenite dikes is still poorly known. In this work, we combined field and petrographic observations with geochemical data on minerals and bulk rocks in order to constrain the primary compositional features of the Cheshmeh-Bid pyroxenites, the geochemical affinities of their parental melts and the possible geodynamic environment during their petrological evolution.

GEOLOGICAL SETTING

Iranian ophiolites represent the remnants of the Neo-Tethyan oceanic lithosphere in the Anatolian segment of the Alpine-Himalayan Orogen (Fig. 1a). They have been divided into five ophiolitic belts (Shafaii Moghadam and Stern, 2015): 1) Late Cretaceous Zagros Outer Belt ophiolites (ZOB) along the Main Zagros Thrust including Kermanshah-Kurdistan, Maku-Khoy-Salmas ophiolites, Khajeh-Jamali ophiolitic massifs (which include the Cheshmeh-Bid ophiolitic Massif),

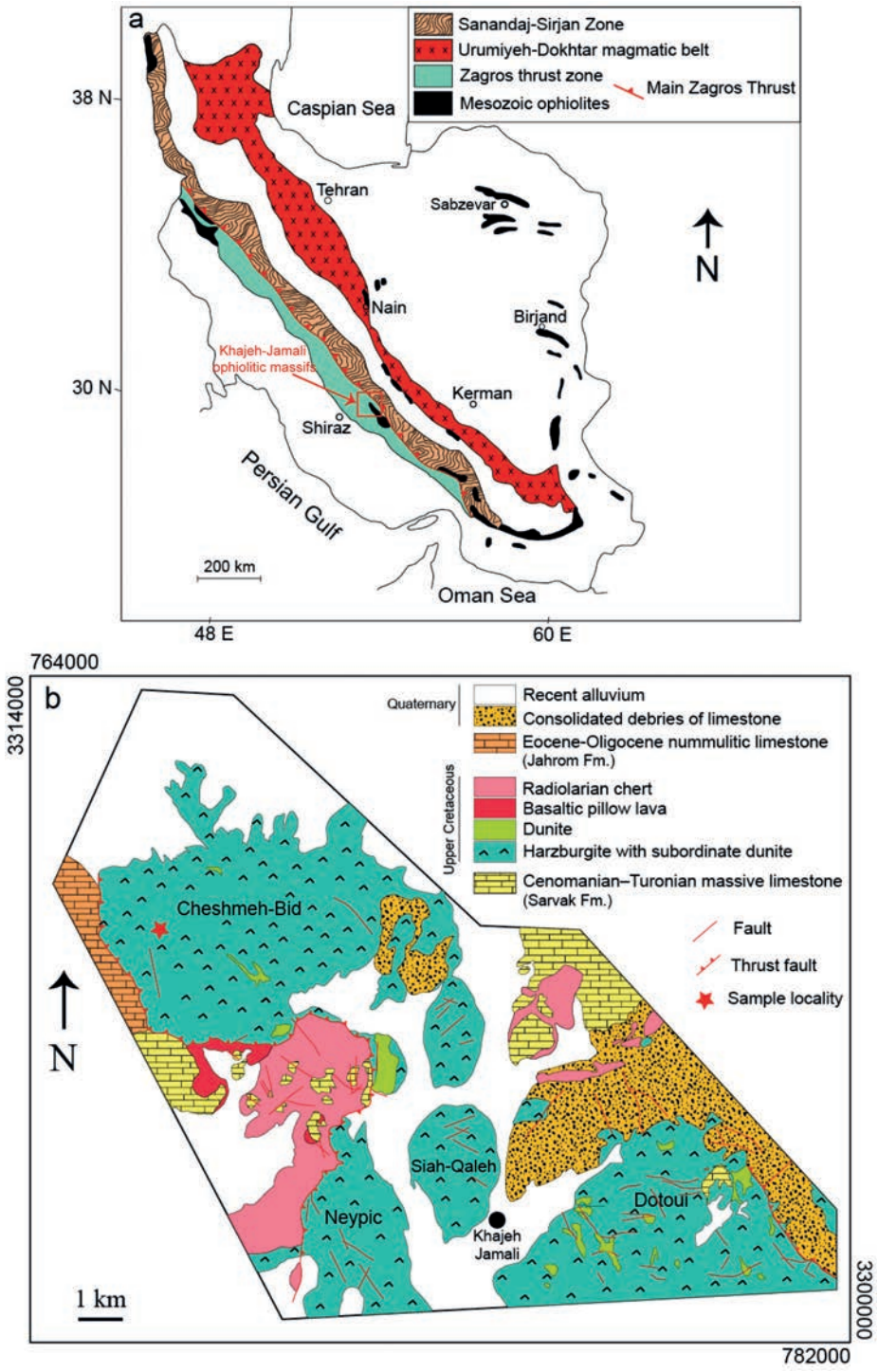

Fig. 1 - (a) Schematic map of Mesozoic ophiolites in Iran; (b) simplified geological map of the Khajeh-Jamali peridotite massifs.

Neyriz and Haji Abad ophiolites; 2) Late Cretaceous Zagros Inner Belt ophiolites (ZIB) including Nain, Dehshir, Shahr-e-Babak and Balvard-Baft ophiolites along the main boundaries of the Central Iranian Micro-continental block; 3) Late Cretaceous-Early Paleocene Sabzevar-Torbate-Heydarieh ophiolites in the northeast of Iran; 4) Early to Late Cretaceous ophiolites including Nehbandan, Birjand and Tchehel-Kureh between the Afghan and Lut blocks; 5) Late Jurassic-Cretaceous Makran ophiolites in the southeast of Iran.

The Khajeh-Jamali massifs consist of four ophiolitic bodies belonging to ZOB ophiolites of the Zagros Mountain in southern Iran, and crop out to the north of Tashk Lake about 20 km from Main Zagros Thrust (Fig. 1a). These massifs are dominantly composed of mantle harzburgite-dunite tectonites and by a Moho Transition Zone (MTZ) (e.g., see Rajabzadeh, 1998; Rajabzadeh and Nazari Dehkordi, 2013; Eslami et al., 2015).

A typical cumulate sequence and a sheeted dyke complex are missing in the Khajeh-Jamali area. The massifs are overlain by a very thin cover of basaltic pillow lavas, reddish-purple radiolarites and radiolarian cherts and Late Cretaceous pelagic limestones (Rajabzadeh, 1998; Eslami et al., 2015). The Cheshmeh-Bid ophiolitic massif are thrust over the Cenomanian/Turonian shallow water deposits of the Sarvak Formation in the western portion of the Khajeh-Jamali area (Alavi, 1994). It is argued that peridotites in the Khajeh-

Jamali area vary from fertile to ultra-refractory, reflected by progressive drop in modal clinopyroxenes moving towards chromite deposits (Rajabzadeh and Moosavinasab, 2012; Rajabzadeh et al. 2013). Monsef et al. (2018) have investigated some peridotites (harzburgites and dunites) in the eastern part of the Cheshmeh-Bid massif (CB). Based on mineral and bulk chemistry, they interpreted clinopyroxene-rich and clinopyroxene-poor harzburgites as variably depleted mantle residues and suggested that clinopyroxene-poor harzburgites along with replacive dunite lenses were generated during fore-arc extension.

The Cheshmeh-Bid ophiolitic massif covers a rugged mountainous area of ~ 25 km^2 in the northwest of the Khajeh-Jamali area (Fig. 1b). This massif hosts large economical concentrations of chromitites with massive and high-grade disseminated texture (Rajabzadeh, 1998; Eslami et al., 2015). The Cheshmeh-Bid peridotites underwent variable degrees of serpentinization. High-Cr podiform chromitite deposits occur within both mantle tectonite and MTZ (Rajabzadeh, 1998; Eslami et al., 2015). It is argued that the Cheshmeh-Bid massive chromitites were related to supra-subduction zone melts with boninitic affinity (e.g., Rajabzadeh, 1998; Eslami et al., 2015).

FIELD OCCURRENCE AND PETROGRAPHIC DESCRIPTION

In the Cheshmeh-Bid ophiolitic massif, pyroxenites occur as straight dikes and dikelets concordant or subconcordant to the foliation of the host mantle peridotites (Fig. 2a). Few pyroxenite dikelets have been also found in the Cheshmeh-Bid chromitite bodies (Fig. 2b). Overall, the boundaries between pyroxenite intrusions and host rocks are rather sharp (Fig. 2a, b). The pyroxenite dikes and dikelets are usually coarse-grained, range in thickness from 2 to 35 cm, and are characterized in the field by dark green to yellowish green colour (Fig. 2a, b). These dykes are usually weathered and variably altered, but in some cases well-preserved pyroxenites are observed.

The Cheshmeh-Bid harzburgites (samples KJDU02, KJDU04, KJDU19) associated to the studied pyroxenites are medium- to coarse- grained rocks with porphyroclastic to granular texture (Fig. 3a). Olivine modal abundance ranges from 70 to 85 vol % with an average grain size between 0.5 and 2 mm. Orthopyroxene modal amount ranges from 15 to 20 vol % with an average grain size between 2 and 3 mm. Coarse-grained (up to 1 mm in size) orthopyroxene porphyroclasts exhibit kink banding and/or undulose extinction. Orthopyroxene porphyroclasts frequently display corroded margins filled by olivine (Fig. 3a). Occasionally, olivine inclusions can be found in the orthopyroxene porphyroclasts (Fig. 3b). Clinopyroxene occurs only as exsolution lamellae in orthopyroxene. Small grains of chromium-rich spinel (0.5 to 2 vol %) range from a few hundred microns to 1 mm and exhibit an interstitial or vermicular habit.

The Cheshmeh-Bid amphibole-bearing orthopyroxenites (amph-orthopyroxenite, samples KJPX03 and KJPX10) are characterized by a porphyroclastic texture defined by coarse-grained (up to 5-6 cm) orthopyroxene (85-90 vol%), amphibole (5-7 vol%), clinopyroxene (2-5 vol%), olivine (< 4 vol%) and spinel (< 3 vol%). Pyroxene porphyroclasts are locally deformed and show mutual exsolutions (clinopyroxene in orthopyroxene and vice versa) (Fig. 3c, d). In some places, clinopyroxene occurs as relics partially resorbed by large blebs of orthopyroxene (Fig. 3e). Fine-grained neoblastic associations of orthopyroxene, clinopyroxene and olivine partially surround the large porphyroclasts (Fig. 3e). Euhedral or subhedral chromite (50 μm to 2.5 mm in diameter) is interstitial or included in both ortho- and clinopyroxene grains (Fig. 3f). Amphibole occurs in three distinct textural sites: (i) euhedral to subhedral magnesium hornblende grains (Fig. 4a), (ii) fine-grained amphiboles associated with orthopyroxene in recrystallized neoblastic assemblages (Fig. 4a), and iii) narrow selvages of tremolite between orthopyroxene and clinopyroxene (Fig. 4b). Talc occurs as retrograde phase around the orthopyroxene grains in the matrix. Tiny flakes of biotite (< 300 μm in diameter) in the matrix appear to be in equilibrium with magnesium hornblende (Fig. 4c).

Orthopyroxenites (samples KJPX01, KJPX07 and KJPX20) show allotriomorphic to porphyroclastic texture. In these samples, orthopyroxene locally grows at the expense of clinopyroxene that occurs mostly as small relics with irregular margins (Fig. 3g). Orthopyroxene grains show equilibrium textures with ~ 120° triple junctions (Fig. 3h).

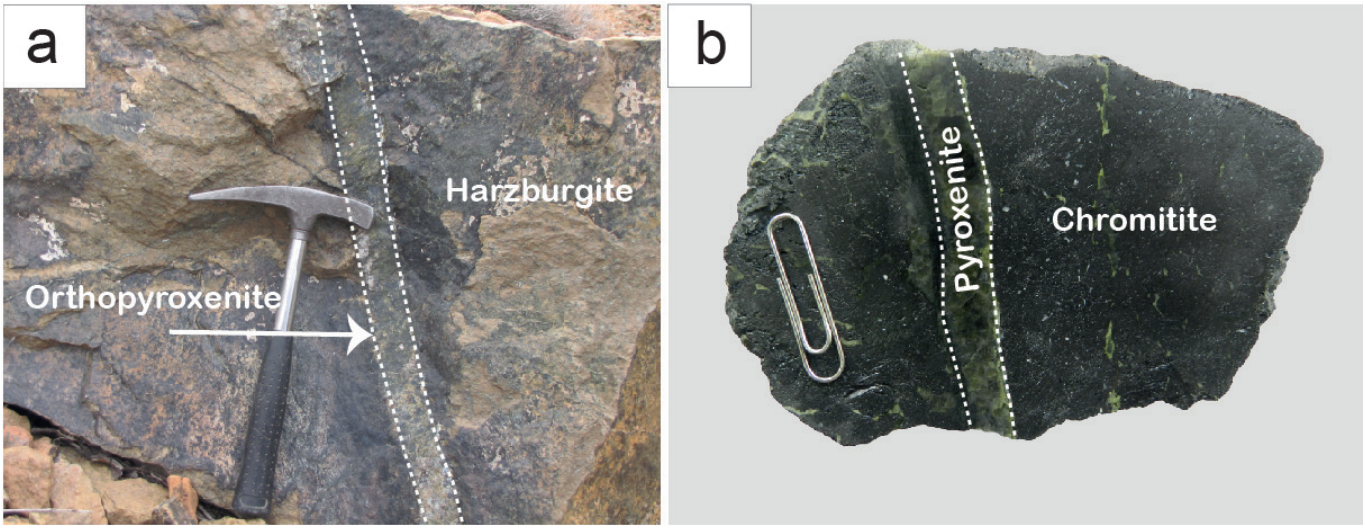

Fig. 2 - Field occurrence of the pyroxenite dykes in the Cheshmeh-Bid peridotite massif: (a) a pyroxenite dykes crosscutting harzburgite; (b) thin pyroxenite dykelet cutting massive chromitite.

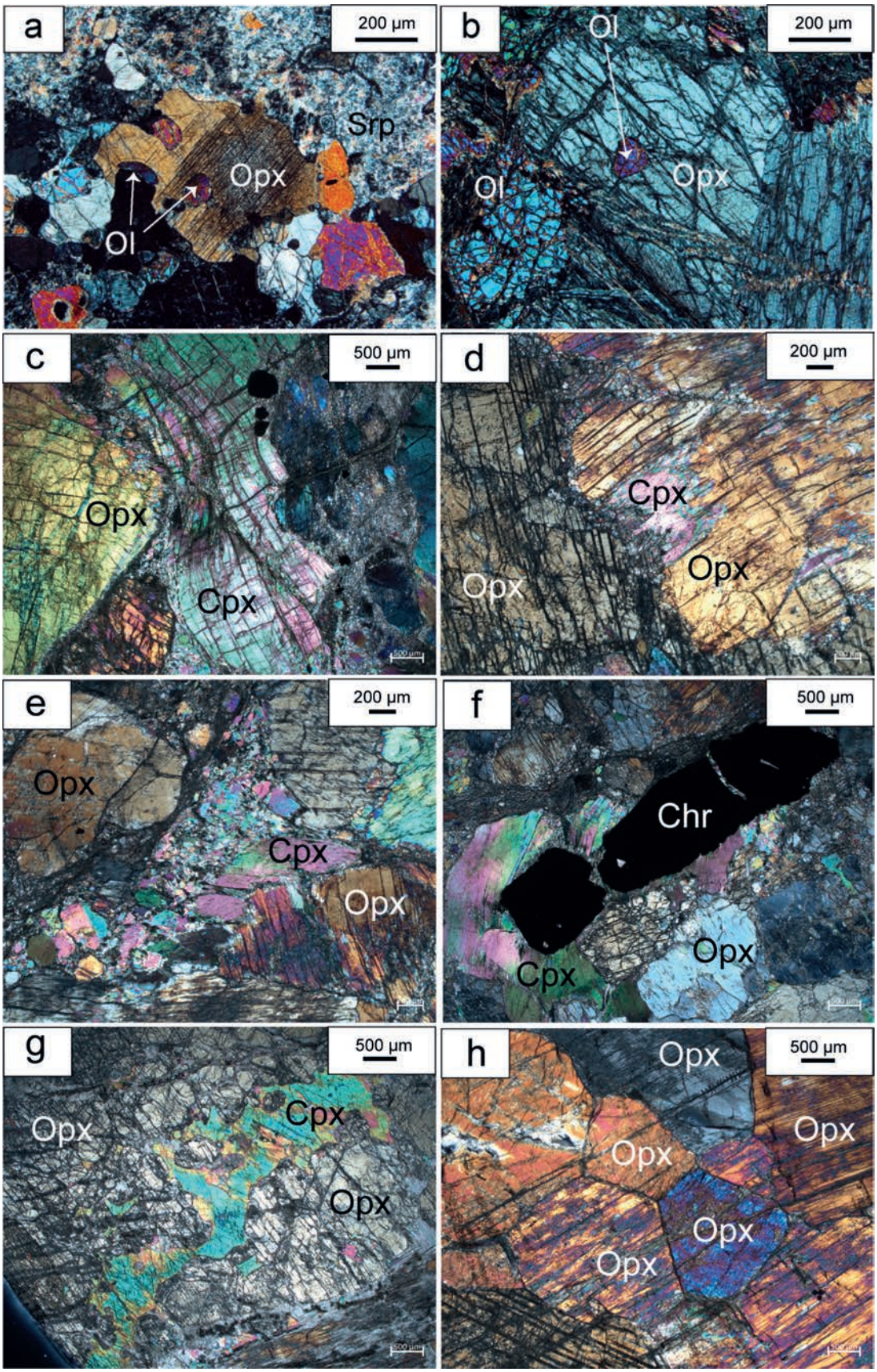

Fig. 3 - Cross polarized (XPL) images showing mineral assemblages and textures of the Cheshmeh-Bid pyroxenites: (a) Opx embayment filled with olivine grains in harzburgite; (b) Olivine inclusion in Opx porphyroclast from harzburgite; (c) deformed Cpx porphyroclast and highly sheared band (amphibole-orthopyroxenite, sample KJPX10); (d) Cpx lamellae exsolved from Opx (amphibole-orthopyroxenite, sample KJPX03); (e) Cpx surrounded by a fine-grained neoblastic assemblage made by Opx + Cpx (KJPX03); (f) subhedral chromite associated with clinopyroxene (amphibole-orthopyroxenite, sample KJPX03); (g) small relics of irregularly shaped Cpx in Opx porphyroclast (orthopyroxenite, KJPX01); (h) triple-junction (~ 120°) grain boundaries between Opx grains (orthopyroxenite, sample KJPX07).

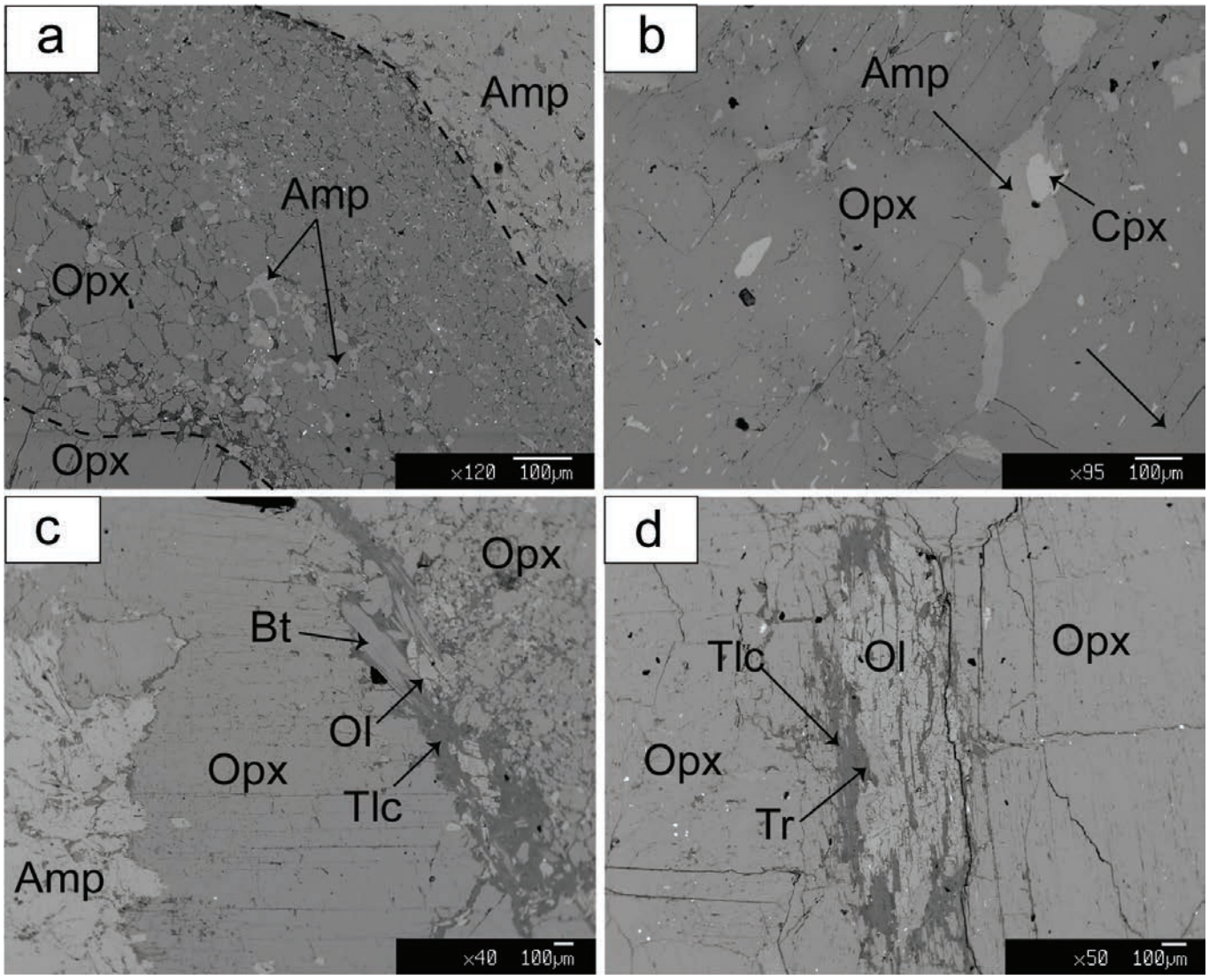

Fig. 4 - Back Scattered Electron (BSE) images showing mineral assemblages of the Cheshmeh-Bid pyroxenites: (a) tremolite selvage between clinopyroxene exsolutions and orthopyroxene (sample KJPX03); (b) recrystallized zone comprising fine-grained amphiboles and orthopyroxenes (amphibole-orthopyroxenite, sample KJPX03); (c) occurrence of a large anhedral amphibole crystal with small subhedral olivine (orthopyroxenite sample KJPX07); (d) secondary assemblages including biotite and talc between orthopyroxene crystals (amphibole orthopyroxenite, sample KJPX10). Opx: Orthopyroxene, Cpx- clinopyroxene; Ol- olivine; Amp- amphibole; Bt- Biotite; Tlc- Talc; Tr- Tremolite.

Local kink bands and undulatory extinction are observed in orthopyroxene porphyroclasts. Olivine occurs as subhedral crystals. Euhedral or subhedral chromite (30 μm to 1 mm in diameter) is observed in both orthopyroxene and clinopyroxene grains. Trace amounts of late magmatic amphibole are associated to orthopyroxene. Secondary assemblages consisting of tremolite, talc and magnetite can be found along the olivine grains and orthopyroxenes (Fig. 4d).

ANALYTICAL METHODS

Polished thin-sections of five fresh pyroxenite samples were examined under transmitted light using a Leica optical microscope at University of Milan. Mineral major element compositions were analysed using a JEOL JXA 8200 Superprobe equipped with five wavelength-dispersive (WDS) spectrometers, an energy dispersive (EDS) spectrometer, and a cathodoluminescence detector (accelerating potential 15 kV, beam current 15 nA), at the Dipartimento di Scienze della Terra, University of Milano. Major elements, Cr and Ni in bulk-rocks were analysed by X-ray Fluorescence (XRF) in a BRUKER S4-Pioneer instrument at the Instituto Andaluz de Ciencias de la Tierra (IACT, Granada, Spain), using standard sample preparation and analytical procedures. The accuracy of analyses was assessed by repeated analyses of international reference material JP-1 (peridotite) handled as unknown, which show good agreement with working values for this standard (Govindaraju, 1994). Whole-rock trace elements (REE, Ba, Th, Pb, Nb, Ta, Sr, Y and Sc) were analysed by an Agilent 8800 QQQ ICP-MS (Inductively Coupled Plasma-Mass Spectrometer) at the Instituto Andaluz de Ciencias de la Tierra (IACT, Granada, Spain). Sample digestion was performed following the $HF/HClO_4$ dissolution procedure described in detail by Ionov et al. (1992), and element concentrations were determined by external calibration using aqueous solutions. Accuracy of the ICP-MS analyses has been assessed analysing the BIR-1 basalt standard as an

unknown during the same analytical runs of the samples. BIR-1 results show good agreement with working values for this reference sample (Jochum et al., 2016).

BULK-ROCK CHEMISTRY

Whole rock major and trace element compositions of pyroxenite and harzburgite samples are reported in Table 1 and Fig. 5. Although we selected the best-preserved samples, the studied pyroxenites and peridotites display variable degree of serpentinization. Pyroxenite samples have L.O.I. ranging from 0.92 to 2.44 wt%. On a volatile-free basis, the pyroxenites display rather high SiO_2 and MgO contents, ranging from 55.82 to 57.07 and 32.77 to 34.40 wt%, respectively, coupled to very low Al_2O_3 and CaO contents, which are lower in the orthopyroxenites (Al_2O_3 = 0.65-1.54 wt. %; CaO = 1.23-1.87 wt%) with respect to the amph-orthopyroxenites (Al_2O_3 = 2.27-2.65 wt%; CaO = 3.04-3.64 wt%) (Fig. 5). TiO_2 and Na_2O are very low and decrease from amph-orthopyroxenites

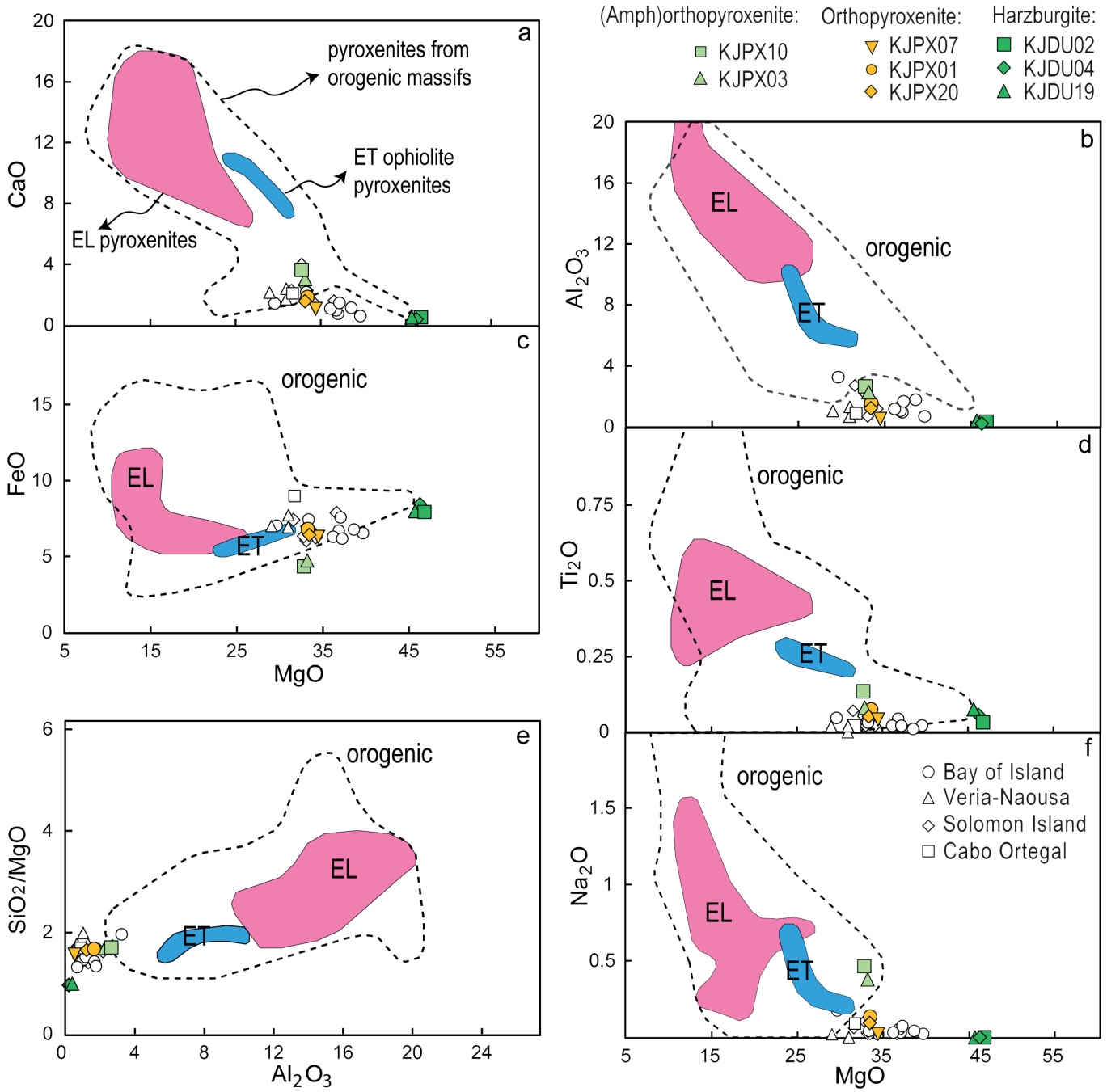

Fig. 5 - (a) MgO versus CaO; (b) Al_2O_3; (c) FeO; (d) TiO_2; (f) Na_2O and, (e) Al_2O_3 versus SiO_2/MgO of pyroxenites. Reference fields for pyroxenites from opholitic and orogenic massifs (Bodinier et al., 1987; 2008; Pearson et al., 1993; Kumar et al., 1996 Garrido and Bodinier, 1999; Mukasa and Shervais, 1999; Takazawa et al., 1999; Morishita and Arai, 2001; Borghini et al., 2016), Erro-Tobbio ophiolite (ET) (Rampone and Borghini, 2008), External Ligurian ophiolites (Montanini et al., 2012; Borghini et al., 2016), subduction-related ophiolite complexes (Varfalvy et al., 1997; Berly et al., 2006; Rogkala et al., 2017), Izu-Bonin-Mariana (IBMP) (Parkinson and Pearce, 1998) and New Caledonia harzburgites (Secchiari et al., 2020) are shown for comparison.

Table 1 - Major (wt%) and trace element compositions (ppm) of the Cheshmeh-Bid pyroxenites and harzburgite.

	Pyroxenite					Serpentinized harzburgite			XRF reference material		ICP-MS reference material	
	Orthopyroxenite			Amphibole-orthopyroxenite					Peridotite		Basalt	
Sample	KJPX01	KJPX07	KJPX20	KJPX10	KJPX03	IRKJDU04	IRKJDU19	IRKJDU02	JP-1	Govindaraju (1994)	BIR-1	Jochum et al. (2016)
Major elements (wt. %)												
SiO_2	53.71	55.89	54.47	53.91	54.83	43.65	42.22	40.65	41.84	42.39		
Al_2O_3	1.48	0.64	1.41	2.56	2.22	0.20	0.37	0.30	0.65	0.62		
FeO	6.41	6.26	6.32	4.19	4.62	8.27	7.45	7.28	7.47	7.50		
MnO	0.16	0.16	0.15	0.11	0.12	0.13	0.12	0.12	0.12	0.12		
MgO	32.06	33.69	32.21	31.65	32.37	45.33	42.64	42.96	44.68	44.72		
CaO	1.79	1.20	1.65	3.52	2.97	0.38	0.48	0.48	0.56	0.56		
Na_2O	0.13	0.04	0.09	0.45	0.37	bdl	bdl	bdl	bdl	0.02		
K_2O	0.05	bdl	0.06	0.06	0.04	bdl	bdl	bdl	bdl	0.003		
TiO_2	0.06	0.05	0.05	0.13	0.06	0.05	0.07	0.03	0.01	na		
P_2O_5	bdl	bdl	bdl	bdl	bdl	bdl	bdl	bdl	bdl	na		
Mg#	90	91	90	93	93	91	91	91				
LOI	2.44	0.92	2.25	1.24	1.07	0	5	6.65	3.89	na		
SiO_2/MgO	1.68	1.66	1.69	1.70	1.69	0.96	0.99	0.95				
Trace elements (ppm)												
Sr	3.96	1.02	3.22	18.37	14.23	3.80	0.24	0.08			99.5	108.6
Y	0.498	0.204	0.515	1.649	1.200	0.025	0.036	0.027			15.3	15.6
Nb	0.193	0.050	0.195	0.679	0.519	0.006	0.017	0.026			0.544	0.553
Ba	5.38	2.53	7.41	3.00	2.27	0.47	0.27	0.15			5.85	6.75
La	0.395	0.049	0.398	0.741	0.551	0.0032	0.0108	0.0041			0.582	0.627
Ce	0.531	0.083	0.529	1.324	0.955	0.0049	0.0176	0.0095			1.79	1.92
Pr	0.055	0.012	0.050	0.162	0.119	0.0007	0.0022	0.0012			0.345	0.3723
Nd	0.165	0.055	0.161	0.683	0.443	0.0051	0.0055	0.0048			2.30	2.397
Sm	0.035	0.013	0.029	0.149	0.109	0.0015	0.0023	0.0013			1.09	1.113
Eu	0.014	0.005	0.012	0.053	0.040	0.0002	0.0007	0.0004			0.522	0.5201
Gd	0.043	0.021	0.040	0.194	0.143	0.0013	0.0017	0.0018			1.99	1.809
Tb	0.008	0.004	0.007	0.033	0.026	0.0003	0.0004	0.0004			0.361	0.3623
Dy	0.065	0.025	0.066	0.251	0.173	0.0027	0.0040	0.0044			2.72	2.544
Ho	0.013	0.008	0.018	0.056	0.040	0.0008	0.0008	0.0010			0.555	0.5718
Er	0.064	0.023	0.058	0.177	0.136	0.0033	0.0043	0.0045			1.67	1.68
Tm	0.012	0.004	0.013	0.028	0.024	0.0011	0.0010	0.0011			0.249	0.2558
Yb	0.093	0.034	0.122	0.241	0.186	0.0104	0.0099	0.0114			1.65	1.631
Lu	0.021	0.007	0.023	0.038	0.035	0.0019	0.0027	0.0026			0.250	0.2484
Ta	0.015	0.011	0.015	0.043	0.032	b.d.l.	0.0032	0.0064			0.0392	0.0414
Pb	0.062	0.120	0.063	0.217	0.178	0.0207	0.726	0.326			2.69	3.037
Th	0.122	0.013	0.161	0.078	0.055	0.0024	0.0049	0.0110			0.0296	0.0328
Sc	17.01	10.33	17.24	24.29	22.17	6.23	7.66	6.61			36.9	43.21

bdl: below detection limit; na: not analyzed

(TiO_2: 0.06-0.13 wt%; Na_2O 0.38-0.47 wt%) to orthopyroxenites (TiO_2: 0.05-0.06 wt%; Na_2O 0.04-0.14 wt%). Amph-orthopyroxenites have Mg-numbers [molar Mg# = Mg/(Mg + Fe^{2+}_{tot}) x 100] around 93, higher than those of the orthopyroxenites (Mg# = 90-91; Table 1). The SiO_2/MgO ratios are relatively low in all the pyroxenite samples.

Host harzburgite samples KJDU02 and KJDU19 have a moderate degree of serpentinization as it can be inferred from LOI values of 6.65 and 5.0 wt%, respectively. Major element bulk-rock compositions of three representative harzburgites are shown in Fig. 5. Compared to the studied pyroxenites, the host harzburgites show much higher MgO and FeO contents (45.68-46.79 and 7.93-8.44 wt%, respectively), and lower SiO_2 (40.65-43.65 wt%), Al_2O_3 (0.2-0.37 wt%) and CaO (0.38-0.48 wt%) concentrations (Table 1; Fig. 5).

Overall, the amph-orthopyroxenites have higher REE contents than orthopyroxenites, whose abundances mostly lie below 1 x C1 (Table 1; Fig. 6a). Amph-orthopyroxenites (samples KJPX03 and KJPX10) show light rare earth element (LREE) enrichment relative to middle REE (MREE) (La_N/Sm_N = 3.20-3.28) with a positive slope from MREE to HREE (Sm_N/Yb_N = 0.65-0.69), resulting in concave-upwards REE patterns (Fig. 6a). Orthopyroxenites (samples KJPX01, KJPX07 and KJPX20) show U-shaped patterns with higher LREE/MREE ratios (La_N/Sm_N = 7.37-8.81) and lower MREE/HREE ratios (Sm_N/Yb_N = 0.27-0.42) than those of amph-orthopyroxenites (Table 1; Fig. 6a). Orthopyroxenite KJPX07 has the lowest REE absolute concentrations (0.1-0.2 x C1) and a relatively flat REE pattern (Fig. 6a). All the pyroxenites show a marked Pb positive anomaly that is more pronounced

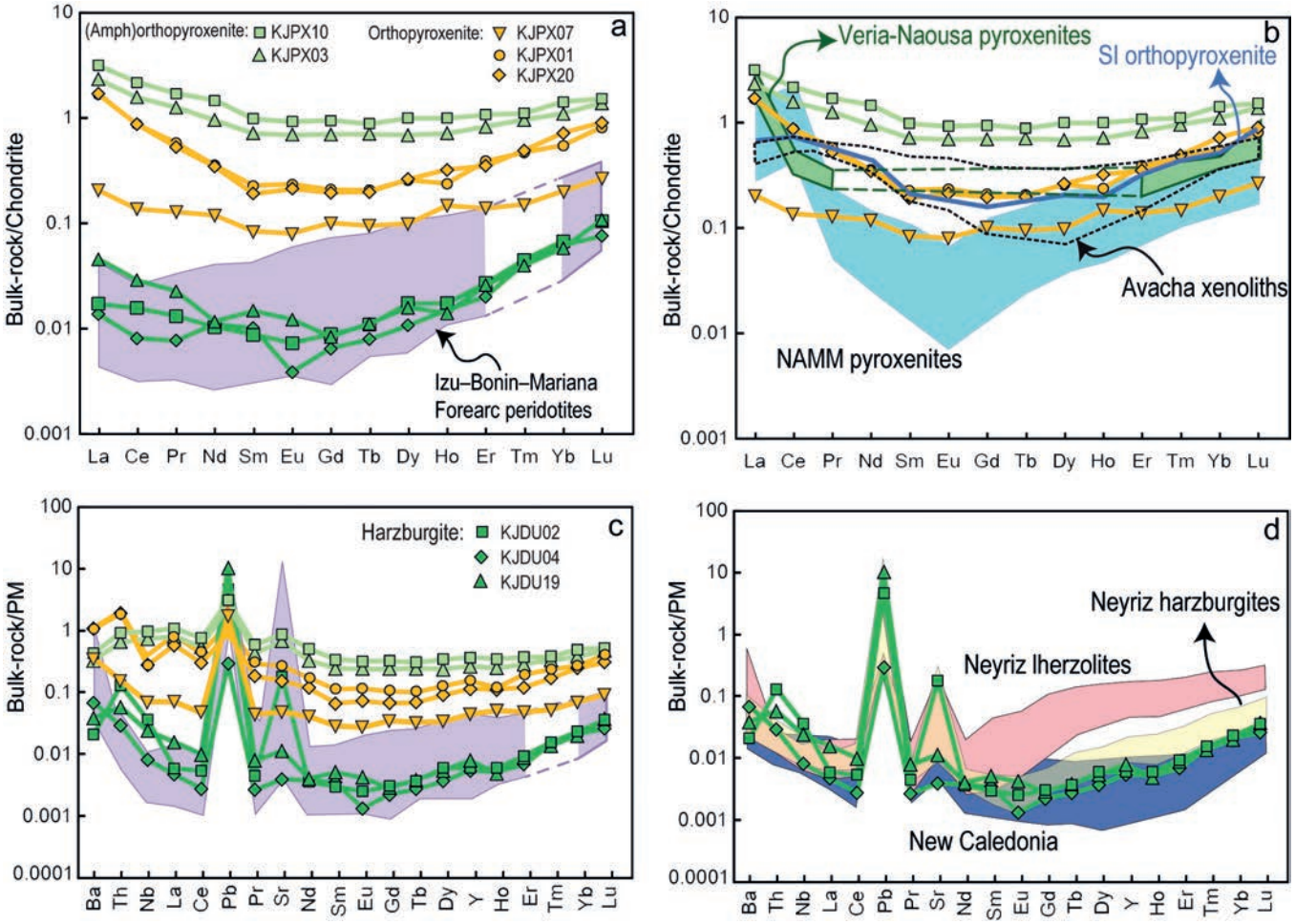

Fig. 6 - (a) Chondrite-normalized REE patterns of the Cheshmeh-Bid pyroxenite dykes (normalizing values from Sun and McDonough, 1989). (b) Primitive mantle normalized multi-element patterns of the Cheshmeh-Bid pyroxenite dykes (normalizing values from Sun and McDonough1989). Data pertaining to the Izu-Bonin-Mariana Forearc peridotites are taken from Parkinson and Pearce (1998). (c) Comparison of chondrite-normalized REE patterns of the Cheshmeh-Bid pyroxenite dykes with Avacha xenoliths from Kamchatka arc (Bénard and Ionov, 2012), orthopyroxenites from Veria-Naousa (Rogkala et al., 2017), Solomon Island (SI) (Berly et al., 2006), North Arm Mountain Massif (NAMM), and Bay of Islands Ophiolite (Varfalvy et al., 1997).

in the orthopyroxenite KJPX07 (Fig. 6c). Amph-orthopyroxenite samples (KJPX03 and KJPX10) display small positive Sr anomalies not observed in the orthopyroxenites (Fig. 6c). As for the REEs, Ba, Th and Nb concentrations are rather low in all the pyroxenites, with PM-normalized values mostly ranging from 0.1 to 1.0 (Fig. 6c).

Harzburgite samples (KJDU2, KJDU4 and KJDU19) have significantly lower REE concentrations compared to the pyroxenites, mostly ranging between 0.01 and 0.001 x C1 (Fig. 6a). They show U-shaped REE patterns with relatively steep slopes from MREE to HREE (Fig. 6a).

Slight Ba and Th enrichments over the REEs, along with prominent Pb and Sr positive anomalies also characterize the Cheshmeh-Bid harzburgites analyzed in this study (Fig. 6c).

MINERAL CHEMISTRY

Orthopyroxene

In Table 2, we reported representative analyses of orthopyroxene from the Cheshmeh-Bid pyroxenites. They are enstatite in composition (Fig. 1S). The Mg# ranges between 0.88 and 0.92 in the orthopyroxenites and 0.91 and 0.93 in the amph-orthopyroxenites (Fig. 7). Orthopyroxenes from orthopyroxenites display CaO contents (0.62-1.05 wt%) higher than those in amph-orthopyroxenites (Fig. 7a), whereas Al_2O_3 and Cr_2O_3 abundances are low for both pyroxenite types (Al_2O_3: 0.40-1.28 wt%; Cr_2O_3: 0.12-0.47 wt%) (Fig. 7b,c). Based on texture, we distinguished two types of orthopyroxene in the amph-orthopyroxenites: (i) coarse porphyroclasts have Mg# ranging from 0.88 to 0.94, variable CaO contents (0.38-1.10 wt%) and Al_2O_3 and Cr_2O_3 contents of 0.90-1.28 wt% and 0.33-0.42 wt%, respectively (Table 2); (ii) orthopyroxene associated with amphiboles in fine-grained neoblastic assemblages is characterized by Mg# values of 0.90-0.94 and low CaO contents (0.17-0.39 wt%); Al_2O_3 and Cr_2O_3 vary between 0.40 and 0.51 wt% and 0.12 and 0.23 wt%, respectively (Table 2, Fig. 7). As a whole, neoblastic orthopyroxenes have lower CaO, Cr_2O_3 and Al_2O_3 compared to orthopyroxene porphyroclasts (Fig. 7).

Clinopyroxene

Representative chemical compositions of clinopyroxene in amph-orthopyroxenite KJPX03 and orthopyroxenite KJPX07 are reported in Table 3. In spite of different microstructural occurrence, they have rather homogeneous diopside

Table 2 - Representative analyses of orthopyroxenes from the Cheshmeh-Bid pyroxenites.

	Coarse-grained					Fine-grained			
	PX20-2	PX01-2	PX10-34	PX07-2	PX03-39	PX10-14	PX10-15	PX03-16	PX03-18
	OP	OP	Amph-OP	OP	Amph-OP	Amph-OP	Amph-OP	Amph-OP	Amph-OP
SiO_2	57.08	57.55	58.10	58.01	58.19	58.35	58.63	58.14	58.20
TiO_2	0.08	0.05	0.04	0.01	0.04	0.01	0.01	bdl	bdl
Al_2O_3	0.90	0.88	0.90	0.70	1.28	0.43	0.50	0.40	0.51
Cr_2O_3	0.43	0.47	0.33	0.40	0.42	0.12	0.23	0.12	0.22
FeO	7.61	7.99	4.99	6.58	4.69	4.53	4.64	5.49	6.11
MnO	0.19	0.17	0.15	0.20	0.11	0.08	0.07	0.17	0.18
MgO	33.16	33.58	35.07	34.28	35.29	36.26	36.19	35.43	35.34
CaO	0.82	0.62	0.91	1.05	0.88	0.30	0.26	0.25	0.21
Na_2O	0.04	0.03	0.01	0.03	0.04	bdl	0.05	0.04	0.03
NiO	0.09	0.07	0.14	0.04	0.16	0.10	0.08	0.08	0.07
Total	100.40	101.42	100.64	101.31	101.11	100.20	100.65	100.12	100.87
Si	1.976	1.974	1.982	1.981	1.973	1.990	1.991	1.993	1.986
$Al^{(IV)}$	0.024	0.026	0.018	0.019	0.027	0.010	0.009	0.007	0.014
$Al^{(VI)}$	0.013	0.010	0.018	0.009	0.024	0.007	0.011	0.009	0.007
Fe_{total}	0.220	0.229	0.142	0.188	0.133	0.129	0.132	0.157	0.174
Cr	0.012	0.013	0.009	0.011	0.011	0.003	0.006	0.003	0.006
Ti	0.002	0.001	0.001	-	0.001	-	-	-	-
Fe^{2+}	0.223	0.225	0.156	0.186	0.145	0.129	0.139	0.161	0.170
Mn	0.006	0.005	0.004	0.006	0.003	0.002	0.002	0.005	0.005
Mg	1.711	1.717	1.783	1.745	1.784	1.843	1.832	1.810	1.798
Ca	0.030	0.023	0.033	0.039	0.032	0.011	0.010	0.009	0.008
Na	0.003	0.002	0.001	0.002	0.003	-	0.003	0.003	0.002
Ni	0.002	0.002	0.004	0.001	0.004	0.003	0.002	0.002	0.002
Total	4.002	4.001	4.009	4.001	4.008	4.000	4.005	4.002	4.001
Mg#	0.88	0.88	0.92	0.90	0.92	0.93	0.93	0.92	0.91
En	0.87	0.87	0.9	0.89	0.91	0.93	0.92	0.91	0.91
Fs	0.11	0.11	0.08	0.09	0.07	0.06	0.07	0.08	0.09
Wo	0.02	0.01	0.02	0.02	0.02	0.01	-	-	-

OP = orthopyroxenite, Amph-OP = amphibole orthopyroxenite. Atomic proportions calculated on the basis of 6 O.

compositions (Fig. 1S), with Mg# ranging between 0.92 and 0.94 (Table 3). They show low Al_2O_3 (0.69-1.57 wt%) and TiO_2 (< 0.07 wt%) abundances coupled to variable Cr_2O_3 (0.51-0.94 wt%) and Na_2O contents (0.25-0.65 wt%).

Olivine

Representative chemical compositions of olivine from the Cheshmeh-Bid orthopyroxenites are displayed in Table 4. Olivine has Mg# ranging from 0.88 to 0.93. NiO and MnO contents vary between 0.23 and 0.42 and 0.10 and 0.21 wt%, respectively. Cr_2O_3 abundance is very low (< 0.03 wt%). The Mg# versus NiO diagram (Fig. 2S) shows that olivine in the Cheshmeh-Bid orthopyroxenites has high Mg# and NiO contents comparable with olivine from dunites and harzburgites investigated by Rajabzadeh and Nazari-Dehkordi (2013) in the same study area.

Cr-rich spinel

Chemical compositions of Cr-rich spinel from the Cheshmeh-Bid pyroxenites are given in Table 5 and shown in Fig. 8. In amphibole-bearing orthopyroxenites, spinels show rather high Cr# [Cr/(Cr + Al)] ranging from 0.71 to 0.73 and Mg# [Mg/(Mg + Fe^{2+})] from 0.58 to 0.64 (Fig. 8a). Spinels from orthopyroxenites have even higher Cr# (Cr# = 0.73-0.80) and lower Mg# (Mg# = 0.40-0.52) (Fig. 8a). The Cr-rich spinels analysed in both orthopyroxenites and amph-orthopyroxenites display low TiO_2 content (< 0.15 wt%) coupled to very low Al_2O_3 contents (< 16 wt%) (Fig. 8b, c).

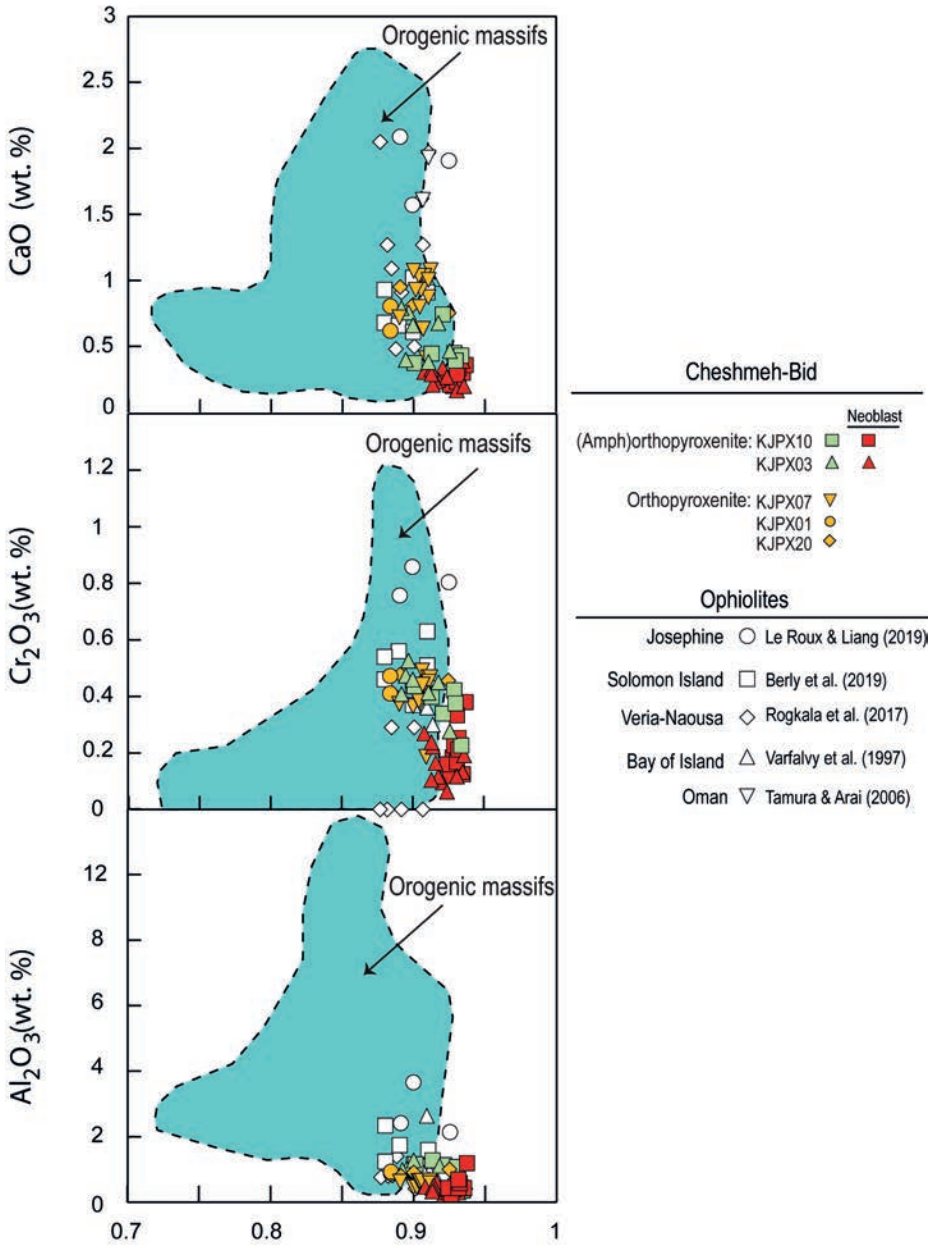

Fig. 7 - Al_2O_3 versus Mg# for: (a) orthopyroxene and (b) clinopyroxene; (c) Cr_2O_3 versus Mg# in clinopyroxene. Reference fields for mantle pyroxenites (Berly et al., 2006), arc-related pyroxenites (Varfalvy et al., 1997; Berly et al., 2006; Rogkala et al., 2017) and Izu-Bonin-Mariana peridotites (IBMP) (Parkinson and Pearce, 1998) are shown for comparison.

Amphibole

Chemical compositions of amphiboles from the Cheshmeh-Bid pyroxenites are given in Table 6. Amphiboles occurring as large grains in amph-orthopyroxenites are magnesium-hornblende (Fig. 3S). They display very high Mg# (0.94-0.98), low TiO_2 (< 0.20 wt%) and high Cr_2O_3 (1.95-2.81 wt%) and Al_2O_3 (8.56-10.24 wt%) abundances. Fine-grained neoblastic amphiboles associated with orthopyroxene and minor clinopyroxene have edenitic compositions characterized by Mg# values of 0.96-0.98, relatively high Cr_2O_3 (1.86-2.28 wt%) and Al_2O_3 (8.22-8.47 wt%) contents and low TiO_2 (< 0.17 wt%) (Fig. 3S). In orthopyroxenite KJPX07, amphiboles occur as small grains in the interstitial matrix and narrow selvages between olivine and orthopyroxenes (Fig. 4d). These amphiboles are tremolites characterized by very high Mg# (0.95-0.97), negligible TiO_2 (< 0.02 wt%) and very low Cr_2O_3 and Al_2O_3 contents ranging between 0.12 and 0.42 and 0.60 and 1.36 wt%, respectively (Fig. 3S).

DISCUSSION

Conditions of intrusion

Field observations indicate that pyroxenites occur as straight dikes and dikelets showing rather sharp contact with the host ultramafic rocks. This suggests that the intrusion of melts from which the pyroxenites crystallized occurred along fractures, evidencing, in turn, that ambient harzburgites and chromitites were in a rather cold regime. Application of Ca-in-Opx thermometer of Brey and Kohler (1990) to the cores of coarse-grained orthopyroxenes in orthopyroxenites yielded temperatures between 906 and 1022°C.

However, these estimates must be considered as minimum temperatures according to the presence of clinopyroxene exsolutions in the coarse orthopyroxenes (Fig. 4b). Indeed, the two-pyroxene thermometer of Brey and Kohler (1990) provides lower temperatures, from 737 to 827°C, presumably related to the cooling of large orthopyroxene porphyroclasts. As expected, the Ca-in-Opx temperatures obtained for the granoblastic orthopyroxenes from fine-grained

Table 3 - Representative analyses of clinopyroxenes from the Cheshmeh-Bid pyroxenites.

Sample No.	IRKJPX07						IRKJPX03	
	Relics of magmatic Cpx						Exsolved Cpx	
SiO_2	54.78	54.40	55.43	55.38	55.82	55.15	54.42	55.16
TiO_2	0.05	bdl	0.01	bdl	0.03	0.04	0.07	bdl
Al_2O_3	0.74	0.75	0.76	0.69	0.70	0.71	1.57	0.93
Cr_2O_3	0.87	0.78	0.84	0.85	0.84	0.80	0.94	0.51
FeO^{total}	1.98	1.83	2.05	2.19	2.07	1.85	2.37	2.03
MnO	0.07	0.10	0.08	0.08	0.07	0.04	0.10	0.08
MgO	17.95	18.04	17.81	17.98	18.03	17.96	16.78	17.62
CaO	23.65	22.49	23.51	23.24	23.72	23.70	22.99	23.49
Na_2O	0.25	0.27	0.32	0.31	0.32	0.31	0.65	0.49
NiO	0.04	0.03	0.02	0.02	0.09	0.01	0.11	0.01
Total	100.38	98.63	100.75	100.67	101.63	100.53	99.99	100.32
Si	1.979	1.982	1.983	1.984	1.984	1.983	1.974	1.990
$Al^{(IV)}$	0.021	0.009	0.009	0.009	0.011	0.014	0.024	0.009
$Al^{(VI)}$	0.011	0.023	0.023	0.020	0.018	0.016	0.043	0.030
Cr	0.025	0.023	0.024	0.024	0.024	0.023	0.027	0.015
Ti	0.001	-	-	-	0.001	0.001	0.002	
Fe^{2+}	0.060	0.081	0.084	0.086	0.078	0.064	0.076	0.063
Mn	0.002	0.003	0.002	0.002	0.002	0.001	0.003	0.002
Mg	0.967	0.980	0.950	0.960	0.955	0.963	0.908	0.948
Ca	0.916	0.878	0.901	0.892	0.903	0.913	0.894	0.908
Na	0.017	0.019	0.022	0.022	0.022	0.022	0.046	0.034
Ni	0.001	0.001	0.001	0.001	0.003		0.003	
Mg#	0.94	0.92	0.92	0.92	0.92	0.94	0.92	0.94
En	0.498	0.505	0.491	0.496	0.493	0.496	0.483	0.494
Fs	0.031	0.042	0.044	0.044	0.04	0.033	0.041	0.033
Wo	0.471	0.453	0.466	0.46	0.467	0.471	0.476	0.473

Atomic proportions calculated on the basis of 6 O.

Table 4 - Representative analyses of olivine from the Cheshmeh-Bid pyroxenites.

Sample No.	IRKJPX10	IRKJPX07					
	Amph-OP	OP					
SiO_2	41.42	41.21	41.19	40.71	41.22	41.16	40.53
TiO_2	bdl	0.03	0.04	bdl	0.01	bdl	bdl
Al_2O_3	bdl	bdl	0.01	0.01	0.02	bdl	0.02
FeO	6.83	11.36	10.99	11.44	9.88	9.98	9.75
MnO	0.10	0.17	0.15	0.21	0.16	0.12	0.15
MgO	52.21	48.78	48.93	49.00	49.62	49.26	48.34
CaO	0.02	bdl	0.02	0.01	0.01	0.04	bdl
Na_2O	bdl	bdl	bdl	0.02	0.01	bdl	bdl
Cr_2O_3	bdl	0.03	bdl	0.01	0.01	0.01	bdl
NiO	0.36	0.32	0.28	0.23	0.41	0.42	0.37
Total	100.95	101.89	101.60	101.64	101.35	100.98	99.19
Si	0.993	0.998	0.999	0.990	0.998	1.000	1.002
Al	-	-	-	-	0.001	-	0.001
Ti	-	0.001	0.001	-	-	-	-
Fe	0.137	0.230	0.223	0.233	0.200	0.203	0.202
Mn	0.002	0.003	0.003	0.004	0.003	0.002	0.003
Mg	1.867	1.762	1.769	1.777	1.791	1.785	1.782
Ca	-	-	0.001	-	-	0.001	-
Na	-	-	-	0.001	-	-	-
Cr	-	0.001	-		-	-	-
Ni	0.007	0.006	0.005	0.005	0.008	0.008	0.007
Total	3.007	3.001	3.000	3.010	3.002	3.000	2.998
Mg#	0.93	0.88	0.89	0.88	0.90	0.90	0.90

Amph-OP = amphibole orthopyroxenite, OP = orthopyroxenite. Atomic proportions calculated on the basis of 4O.

Table 5 - Representative major element compositions of chromian spinels from the Cheshmeh-Bid pyroxenites.

	Amphibole-orthopyroxenite					Orthopyroxenite	
	PX10			PX03		PX07	PX20
SiO_2	0.02	0.02	0.06	0.05	0.03	0.06	0.05
TiO_2	0.06	0.09	0.11	0.09	0.15	0.12	0.11
Al_2O_3	15.10	15.30	13.95	14.10	15.06	11.36	13.74
Cr_2O_3	53.99	54.72	56.61	56.82	55.70	58.42	54.39
FeO*	18.75	19.11	17.30	16.74	17.25	22.59	21.91
MnO	0.09	0.12	0.08	0.11	0.24	0.20	0.09
MgO	12.46	12.40	13.27	13.87	13.44	8.65	10.88
CaO	bdl	bdl	0.04	0.02	bdl	0.01	0.02
NiO	0.14	0.07	0.19	0.14	0.15	0.10	0.07
Total	100.61	101.85	101.65	101.99	102.03	101.53	101.27
Si	0.001	0.001	0.002	0.001	0.001	0.002	0.002
Ti	0.001	0.002	0.003	0.002	0.004	0.003	0.003
Al	0.568	0.569	0.520	0.522	0.556	0.440	0.524
Cr	1.363	1.365	1.414	1.409	1.379	1.518	1.390
Fe_{tot}	0.501	0.504	0.457	0.439	0.452	0.621	0.592
Fe^{2+}	0.415	0.424	0.379	0.357	0.377	0.577	0.485
Fe^{3+}	0.085	0.079	0.075	0.081	0.074	0.044	0.105
Mn	0.002	0.003	0.002	0.003	0.006	0.005	0.003
Mg	0.593	0.583	0.625	0.649	0.627	0.424	0.524
Ca	-	-	0.001	0.001	-	-	0.001
Ni	0.003	0.001	0.004	0.003	0.003	0.002	0.002
total	3.533	3.533	3.484	3.471	3.479	3.638	3.629
$Fe^{2+}/(Fe^{2+}+Mg)$	0.41	0.42	0.38	0.36	0.38	0.58	0.48
$Fe^{3+}/(Fe^{3+}+Al+Cr)$	0.04	0.04	0.04	0.04	0.04	0.02	0.05
Mg#	0.59	0.58	0.62	0.64	0.62	0.42	0.52
Cr#	0.71	0.71	0.73	0.73	0.71	0.78	0.73

Atomic proportions calculated on the basis of 4 (O).

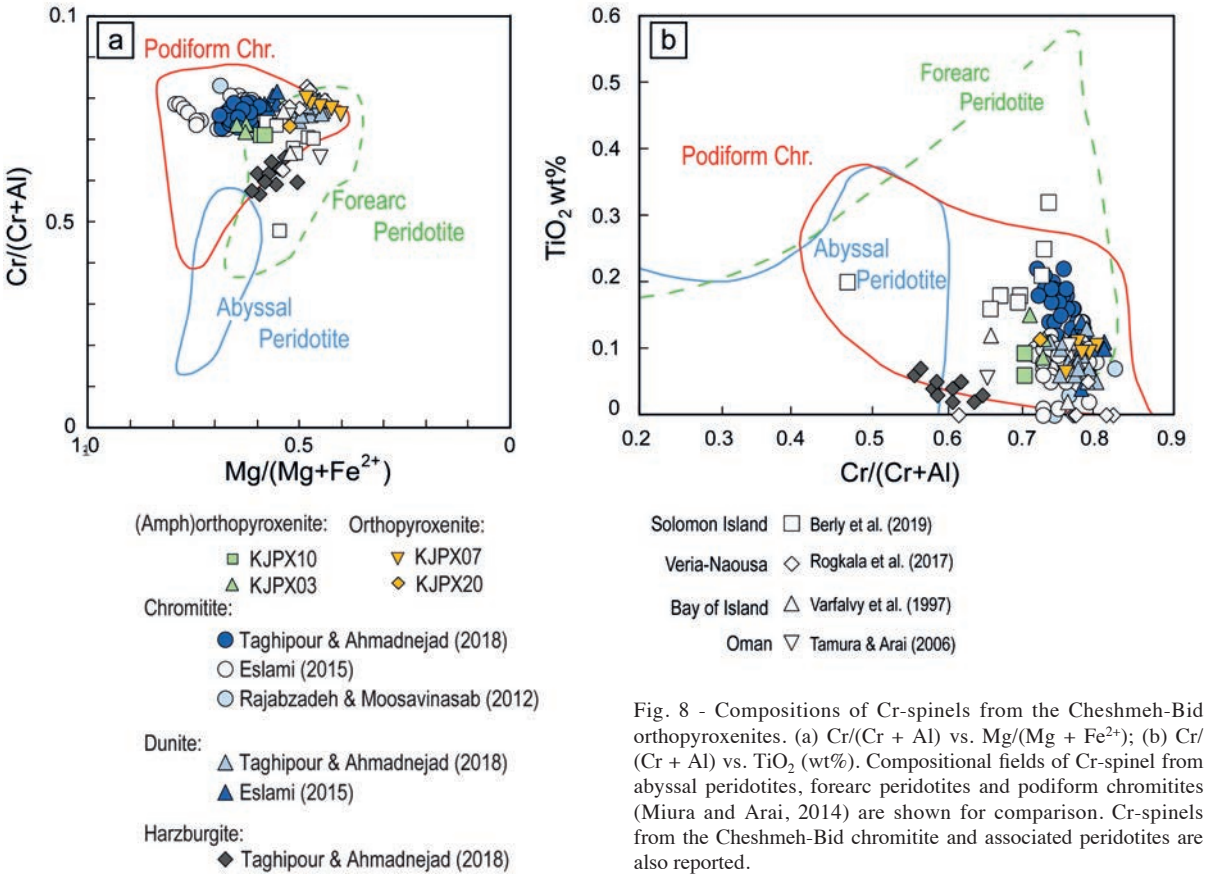

Fig. 8 - Compositions of Cr-spinels from the Cheshmeh-Bid orthopyroxenites. (a) Cr/(Cr + Al) vs. Mg/(Mg + Fe^{2+}); (b) Cr/(Cr + Al) vs. TiO_2 (wt%). Compositional fields of Cr-spinel from abyssal peridotites, forearc peridotites and podiform chromitites (Miura and Arai, 2014) are shown for comparison. Cr-spinels from the Cheshmeh-Bid chromitite and associated peridotites are also reported.

recrystallized assemblages are still lower, ranging from 688 to 771°C (Table 7).

We also applied the geothermometer of Putirka (2016) to derive the temperature estimates for the amphibole crystallization in the Cheshmeh-Bid pyroxenites (Table 7). Calculations show that Mg-hornblende and edenitic amphiboles give average equilibrium T of 909 °C (+/-19) and 874°C (+/-18), respectively, suggesting a late stage magmatic origin.

The occurrence of spinel, and lack of plagioclase or garnet, within the primary mineral assemblage of these ultramafic pyroxenites suggests moderate pressure of intrusion (Borghini and Fumagalli, 2018). Bulk compositions of Cheshmeh-Bid pyroxenites are not significantly different from those of peridotites in terms of Na_2O and CaO contents (Table 1). Their normative Albite/Diopside (Ab/Di) ratio varies within 0.10-0.26 for the orthopyroxenites, mostly covering

Table 6 - Representative analyses of amphiboles from the Cheshmeh-Bid pyroxenites.

	Orthopyroxenite				Amphibole-orthopyroxenite				
	IRKJ01	IRKJ07			IRKJ03		IRKJPX10		
Amphibole types	Edenite	Tremolite			Mg-Hbl	Edenite	Mg-Hbl		Edenite
SiO_2	51.80	58.74	57.49	58.46	48.66	49.43	47.86	47.21	50.55
TiO_2	0.12	0.02	bdl	bdl	0.19	0.13	0.20	0.19	0.17
Al_2O_3	6.77	0.60	1.36	0.59	9.00	8.47	8.56	10.24	8.22
Cr_2O_3	1.04	0.26	0.42	0.12	2.66	2.28	1.95	2.81	1.86
MnO	0.04	0.09	0.04	0.03	0.03	0.09	0.03	bdl	0.05
FeO	3.44	3.35	2.01	2.18	2.45	2.35	2.26	2.49	2.12
NiO	0.12	0.14	0.13	0.10	0.10	0.12	0.19	0.18	0.11
MgO	20.70	25.87	23.63	23.02	19.85	20.08	19.94	19.74	20.78
CaO	11.63	9.41	12.69	13.17	11.86	12.07	11.45	11.95	11.90
Na_2O	1.46	0.26	0.24	0.10	2.23	1.92	2.38	2.48	1.75
K_2O	0.25	0.02	0.00	0.00	0.46	0.26	0.49	0.54	0.28
Total	97.37	98.77	98.00	97.78	97.48	97.21	95.30	97.83	97.80
T (ideally 8 apfu)									
Si	7.184	7.896	7.819	7.977	6.842	6.920	6.853	6.626	6.995
Al	0.816	0.095	0.181	0.023	1.158	1.080	1.147	1.374	1.005
Ti		0.002							
Fe^{3+}		0.007							
C (ideally 5 apfu)									
Ti	0.012				0.020	0.014	0.021	0.021	0.018
Al	0.290	0.000	0.036	0.072	0.334	0.318	0.298	0.320	0.335
Cr	0.114	0.028	0.045	0.012	0.296	0.252	0.221	0.312	0.203
Fe^{3+}	0.269	0.081	0.100			0.142	0.137	0.146	0.167
Ni	0.013	0.015	0.014	0.011	0.011	0.014	0.022	0.020	0.013
Fe^{2+}	0.022		0.014	0.222	0.179	0.068	0.045	0.052	
Mg	4.280	4.876	4.791	4.682	4.161	4.191	4.257	4.130	4.263
Mn^{2+}	0.005	0.010	0.004	0.004	0.004	0.010	0.003		0.006
Fe^{2+}	0.108	0.288	0.115	0.027	0.109	0.065	0.089	0.095	0.078
Mg		0.308							0.024
B (ideally 2 apfu)									
Ca	1.728	1.355	1.849	1.925	1.787	1.811	1.757	1.797	1.764
Na	0.159	0.039	0.032	0.026	0.100	0.115	0.151	0.108	0.128
A (from 0 to 1 apfu)									
Na	0.234	0.029	0.032	0.000	0.508	0.407	0.510	0.567	0.341
K	0.044	0.003		0.001	0.082	0.047	0.089	0.097	0.049
Sum T,C,B,A	15.278	15.032	15.032	14.982	15.591	15.454	15.600	15.665	15.389

Structural formula was recalculated on the basis of 22 O.

Table 7 - Geothermometric estimates (°C) based on major elements.

	Brey & Kohler (1990)		Taylor (1998)	Putirka (2016)
Sample	T(Cpx-Opx)	T(Ca-in-Opx)	T(Cpx-Opx)	T (amp)
KJPX01		906		835
KJPX03	805	688-985	765	847-916
KJPX07	854-893	1022	741-830	
KJPX10		748-993		882-951
KJPX20		968		

the Ab/Di range of several model lherzolites (Ab/Di = 0.15-0.30; Fumagalli et al., 2017). Amph-orthopyroxenites have higher Ab/Di ratios (0.38-0.39); this indicates that the stability of plagioclase in these rocks would be expected to be at pressure higher than peridotites, as demonstrated by experiments on model lherzolites (Green and Falloon, 1998; Borghini et al., 2010; 2011; Fumagalli et al., 2017). However, the occurrence of amphibole can partially limit the stability of plagioclase in ultramafic rocks (Niida and Green, 1999). Although the two phases often coexist in mantle pyroxenites (e.g. Adam et al., 1992; Montanini et al., 2006; Borghini et al., 2016), the stability of plagioclase, amphibole-bearing assemblage in pyroxenites, as a function of the bulk water content, has been not still experimentally investigated. Anyway, taking into account for the very high Ab/Di ratios of amph-orthopyroxenites, the pressure of Cheshmeh-Bid pyroxenites emplacement may be realistically fixed at $P > 1$ GPa. On the other hand, the lack of garnet limits the pressure of intrusion at $P < 1.5$ GPa, as experimentally determined for a high-MgO pyroxenite (Borghini and Fumagalli, 2018).

Chemistry of pyroxenite parental melts

Pyroxenites have been documented from several orogenic and ophiolitic massifs and they define a broad range in bulk-rock major element compositions. As most of these pyroxenites resulted from high-pressure melt segregation, which may be combined to melt-peridotite interaction to some extent (e.g., Garrido and Bodinier, 1999; Marchesi et al., 2013; Montanini et al., 2015; Borghini et al., 2016; Tilhac et al., 2016), bulk-rock compositions roughly reflect the final modal abundance. In turn, the latter is indicative of the parental melt chemistry that is usually related to the geodynamic setting of their source region.

In Fig. 5, we compare the compositions of Cheshmeh-Bid pyroxenites with the compositional fields defined by pyroxenites from ophiolitic and orogenic massifs. In addition, we show the data from selected orthopyroxene-rich pyroxenites from ophiolites originated in subduction settings that were interpreted as crystallization products from melts with a boninite-like signature.

Very low Al_2O_3, CaO, Na_2O and TiO_2 abundances coupled to relatively high MgO and SiO_2 contents (Fig. 5) reflect high orthopyroxene modal abundances of the Cheshmeh-Bid pyroxenites. Accordingly, their bulk-rock compositions plot near the Enstatite join within the pseudoternary system forsterite (Fo)-Ca-Tschermak (CaTs)-quartz (Qtz) projected from diopside (Di) (Fig. 9). These bulk-rock compositions consistently overlap those of orthopyroxene-rich pyroxenites embedded in ultramafic massifs from Bay of Island (Varfalvy et al., 1997), Veria-Naousa (Rogkala et al., 2017), Cabo Ortegal (Tilhac et al., 2016), and Solomon Islands (Berly et al., 2006) (Figs. 6 and 9).

Berly et al. (2006) argued that pyroxenites from Solomon Islands were formed through the interaction of an aqueous fluid and a harzburgitic upper mantle in a supra-subduction zone. For the other study cases, the origin of pyroxenites was ascribed to the interaction of Si-rich (boninite-like) melts with mantle depleted peridotites in an arc-related environment (Varfalvy et al., 1997; Tilhac et al., 2016; Rogkala et al., 2017). The crystallization of high-MgO silica-rich melts (boninites) generated orthopyroxene-rich pyroxenite dikes in mantle peridotite from North Arm Mountain massif (Bay of Island ophiolite, Newfoundland; Varfalvy et al., 1997).

The involvement of boninite-like melts in the origin of CB pyroxenites is also suggested by the mineral chemistry. Spinels from the studied pyroxenites have very high X_{Cr} coupled to low TiO_2 contents that are typical of spinels in podiform chromitites and forearc peridotites from literature (Fig. 8a, b; e.g., Eslami et al., 2015; Grieco et al., 2018). Moreover, orthopyroxenes from CB pyroxenites have major element compositions similar to those in pyroxenites crystallized by boninite melts, in terms of X_{Mg} values, CaO, Cr_2O_3 and Al_2O_3 contents (Fig. 7).

Fig, 6b shows that bulk-rock REE patterns of the studied pyroxenites are similar to orthopyroxene-rich pyroxenites from Veria-Naousa ophiolites (Rokgala et al., 2017), North Arm Mountain Massif (NAMM, Varfalvy et al., 1997), Avacha xenoliths (Bénard and Ionov, 2012), and Solomon Islands (Berly et al., 2006). All these pyroxenites display U-shaped REE patterns that, coupled to high MgO and SiO_2 contents and low Al_2O_3 and TiO_2 abundances, are consistent with a boninite-like signature of the parental melts (e.g., Varfalvy et al., 1997). In particular, Bénard and Ionov (2012) argued that such REE patterns can result from olivine-melt reaction at decreasing melt mass, as supported by numerical simulation of Bodinier et al. (1990). They suggested that orthopyroxenite veins within harzburgite xenoliths from Kamchatka derived from the interaction between refractory harzburgite and low-Ca boninites generated by fluid-fluxed melting of a previously depleted mantle source. A similar origin has been also proposed for the pyroxenites from Cabo Ortegal massif (Tilhac et al., 2016) and Veria-Naousa ophiolites (Rogkala et al., 2017). These pyroxenites show selective LILE enrichment and positive Pb and Sr anomalies that we also observed in CB pyroxenites and in their host harzburgites (Fig. 6c). As shown in Fig. 4S, there are no discernible correlation between LOI, LREE and fluid-mobile elements like Pb and Sr.

Based on bulk-rock compositions and mineral chemistry, we infer that CB pyroxenites originated from the intrusion and crystallization of hydrous Si-rich, low-Ca melts with a boninite signature. Such chemical affinity could be inherited either from partial melting of refractory peridotites in a supra-subduction environment or through melt differentiation driven by the interaction with the ambient harzburgites (e.g., Tilhac et al., 2016). Accordingly with this latter scenario, the bulk-rock trace element compositions of harzburgite hosting the CB pyroxenites well match those of Izu-Bonin-Mariana Forearc peridotites (Fig. 6c).

In order to obtain the REE composition of the pyroxenite parental liquid, we applied the model of Bédard (1994) starting from the bulk-rock trace element composition and modal abundances of orthopyroxenite KJPX07 and amph-orthopyroxenite KJPX03. The model assumes that all the minerals occurring in the rock crystallized in equilibrium from the same melt, possibly retaining a trapped melt fraction, and that no post-cumulus metasomatism occurred. Results and details of parameters used in the model are reported in Table 1S and Fig. 10. Calculated melts have REE patterns compatible with low-CaO boninites from classical localities (Bonin Islands, Taylor et al., 1994; Cape Vogel-Papua, Kamenetsky et al., 2002; New Caledonia:, Cluzel et al., 2016). In particular, model liquids for KJPX03 fall in the wide range of boninites for trapped melt TM > 8-10%, and TM < 6-8% for sample KJPX07 (Fig. 10). It is noteworthy that the REE concentrations of the calculated pyroxenite-forming melts for a given trapped melt fraction TM are higher for sample KJPX03 with respect to sample KJPX07 (Fig. 10). This could imply that the pyroxenites crystallized from similar liquids but contained different amounts of trapped melts (higher for the amphibole-bearing sample

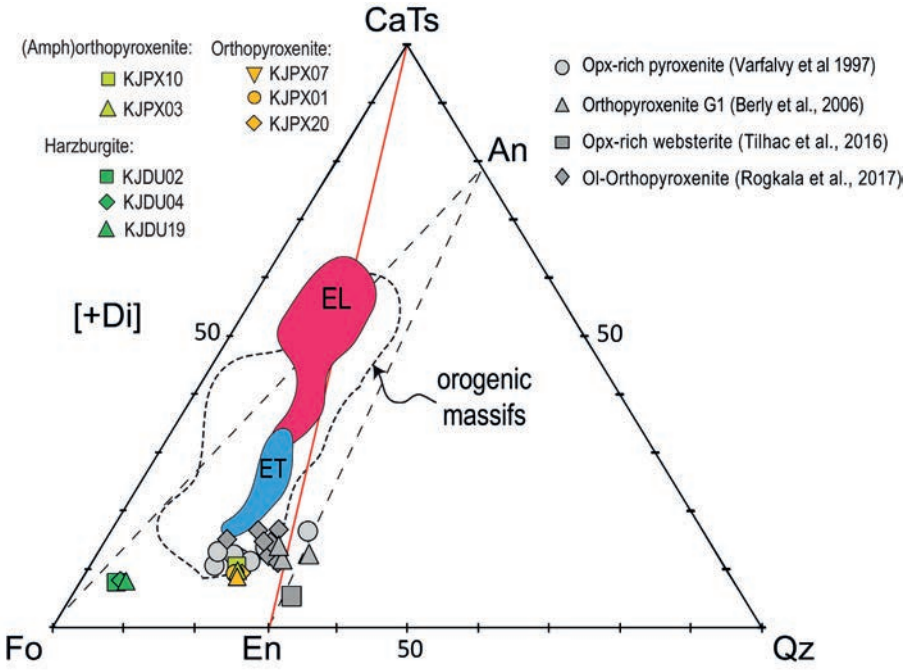

Fig. 9 - Whole-rock normative compositions of the Cheshmeh-Bid pyroxenites and harzburgites projected from diopside within the CMAS plane forsterite-calcium Tschermak-quartz (Fo-CaTs-Qz) (O'Hara, 1968).

KJPX03, in agreement with its higher contents of REE and other incompatible trace elements in the bulk rock). Model liquids for KJPX03 fall in the wide range of boninites for trapped melt TM > 8-10%, and TM < 6-8% for sample KJPX07 (Fig. 10). The REE compositions of the two resulting liquids mostly differ in the M- to HREE fractionation, i.e. normalized patterns are nearly flat for KJPX07, and negatively fractionated for KJPX03 (Fig. 10). This could reflect the role of late stage crystallization of amphibole in the sample KJPX03. Overall, the results of this model, in agreement with the bulk-rock and mineral chemistries discussed above, strongly support that the CB pyroxenites derived from boninitic liquids.

Significance of the Cheshmeh-Bid mantle section in the evolution of the Neyriz ophiolites

The Chesmeh-Bid harzburgites are highly depleted rocks, as attested by the lack of clinopyroxene, coupled to very low Al_2O_3 and CaO bulk contents. Their REE and PM-normalized trace element patterns (Fig. 6) are similar to well-known occurrences of residual peridotites from modern and fossil forearc settings (e.g., Izu-Bonin-Mariana: Parkinson and Pearce, 1998; New Caledonia ophiolite: Marchesi et al., 2009; Secchiari et al., 2020). For the Neyriz harzburgites, Shafaii Moghadam et al. (2014) computed degrees of melting in the range 15-20% based on Cr# of spinel coupled with Fo content of olivine. Higher degrees of melting (~ 20-22%) can be estimated for the harzburgites of this study comparing their bulk rock HREE composition (namely Yb and Lu abundances of 0.02-0.04 times primitive mantle) with those of New Caledonia harzburgites for which a fractional melting model in the spinel stability field was applied (see Secchiari et al., 2020). Such high degrees of melting, which can ultimately lead to clinopyroxene exhaustion, can be promoted by significant lowering of solidus temperature due to H_2O-influx from the slab in a subduction-related setting. This is also consistent with comparatively high abundances of FME (fluid-mobile elements, e.g., Ba, Sr, Pb), LREE and MREE (Fig. 6) in the harzburgites, which do not seem consistent with a simple history of anhydrous partial melting and require a more complex

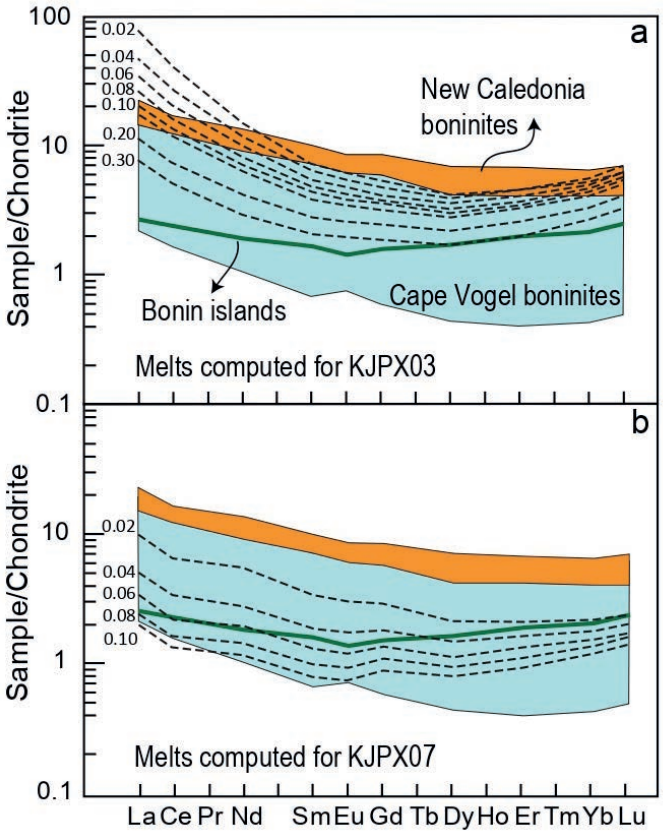

Fig. 10 - Chondrite-normalized REE patterns representing calculated melts in equilibrium with pyroxenite samples KJPX03 and KJPX07. Normalization values of chondrite Cl are from Sun and McDonough (1989). REE patterns of boninites from Bonin islands (Taylor et al., 1994), Cape Vogel-Papua (Kamenetsky et al., 2002) and New Caledonia (Cluzel et al., 2016) are also displayed for comparison. REE modelling of the parental liquid compositions were carried out according to the procedure of Bédard (1994), that is based on whole-rock trace element concentrations assuming variable amounts of trapped melt. Numbers on the patterns refer to trapped melt percentages. Partition coefficients employed for REE modelling are reported in Table 1S. Mineral mass fractions of olivine, spinel, opx, cpx and amphibole considered for the calculations are the modal compositions of the two pyroxenites obtained by mass balance calculations (see Table 1S).

evolution. FME enrichments may be the result of addition during fluid-assisted melting (e.g., Shervais and Jean, 2012; Secchiari et al., 2020) as well as of post-melting metasomatism. In the latter scenario, the U-shaped REE patterns of highly refractory harzburgites have been interpreted as due to percolation and entrapment at depth of small amounts of depleted silicate melts with very low HREE contents like boninites (Parkinson and Pearce, 1998; Rajabzadeh and Nazari-Dehkordi, 2013; Secchiari et al., 2020).

Presence of olivine embayment within orthopyroxene porphyroclasts in the Cheshmeh-Bid harzburgites may be related to incongruent melting of orthopyroxene, which produces olivine during decompression melting in supra-subduction zone settings or beneath ocean ridges (Niu, 1997). Such dissolution-replacement process can be augmented by the reaction with an upward migrating melt percolating through the residual peridotites. In fact, it has also been argued that these resorption textures can be the result of reactive porous flow process (e.g., Seyler et al., 2007; Rampone et al., 2008; 2020) or open-system porous flow migration and interaction of pyroxene-undersaturated melts with residual peridotites (e.g., Dijkstra et al., 2003, Piccardo and Vissers, 2007; Rampone et al., 2008).

During NE-dipping subduction of northern margin of the Neo-Tethyan oceanic lithosphere, a forearc/protoarc crust formed in the Zagros (e.g., Shafaii Moghadam et al., 2014; Monsef et al., 2018). The evolution of the investigated pyroxenite-bearing mantle section may be reconciled within this geodynamic framework. Extensive partial melting triggered by slab-related aqueous fluids left highly refractory mantle residues which were then affected by reactive porous flow of pyroxene-undersaturated melts producing partial orthopyroxene resorption (see also Zanetti et al., 2006). These melts may have been responsible for the post-melting enrichment in incompatible elements observed in the harzburgites. At a later stage, injection of hydrous melts with boninitic affinity led to formation of chromitites (Rajabzadeh and Moosavinasab, 2012; Eslami et al., 2015; Taghipour and Ahmadnejad, 2018). Finally, at relatively colder thermal conditions, both harzburgite and chromitite were intruded by boninitic melts that yielded the studied dikes and dikelets of orthopyroxenites and amphibole-bearing orthopyroxenites. These pyroxenites represent, therefore, the products of the final stage of melt percolation and intrusion recorded by the Neyriz mantle sector during their evolution in the ancient forearc setting. Magmatic textures of the pyroxenites were finally overprinted by ductile deformation and solid-state recrystallization presumably related to the exhumation of Neyriz ophiolites.

CONCLUDING REMARKS

The Cheshmeh-Bid orthopyroxenites occur as dikes and dikelets intruding strongly depleted harzburgites. Small amounts of magmatic amphibole are locally observed in the pyroxenites. Bulk-rock major element composition display low Al_2O_3, CaO, Na_2O and TiO_2 abundances coupled to relatively high MgO and SiO_2 contents. Whole-rock trace element data show low REE absolute contents and U-shaped REE patterns, moderate LILE enrichment and positive Pb and Sr anomalies. Mineralogical and geochemical data in conjunction with petrographic evidences point to crystallization from hydrous Si-rich, low-Ca melts with a boninite signature. Melt injection most probably occurred in an intra-oceanic forearc system during cooling and decompression of the host harzburgites in a lithospheric regime. The Chesmeh-Bid orthopyroxenites were subsequently affected by ductile deformation and solid-state recrystallization during exhumation of the Neyriz ophiolite.

ACKNOWLEDGMENTS

We would like to express our sincere gratitude to local people in Khajeh-Jamali village and workers from the Fars Chromite Company. Andrea Risplendente (University of Milan) is thanked for his help during the electron microprobe measurements. C.M.'s research has been funded by project PID2019-111715GB-I00 / AEI / 10.13039/501100011033 and partially with the support of the Italian Ministry of Education (MIUR) through the projects "PRIN2017 - Mineral reactivity, a key to understand large-scale processes (2017L83S77)" and "Dipartimenti di Eccellenza 2018-2022". Comments by Quing Xiong and an anonymous reviewer, and careful editorial handling by Chuan-Zhou Liu are much appreciated.

REFERENCES

Adam J., Green T.H. and Day R.A., 1992. An experimental study of two garnet pyroxenite xenoliths from the Bullenmerri and Gnotuk Maars of western Victoria, Australia. Contrib. Miner. Petrol., 111: 505-514.

Alavi M., 1994. Tectonics of the Zagros orogenic belt of Iran: new data and interpretations. Tectonophysics, 229: 211-238.

Allègre C. J. and Turcotte D. L., 1986. Implications of a two-component marble-cake mantle. Nature, 323: 123-127.

Bédard J.H., 1994. A procedure for calculating the equilibrium distribution of trace elements among the minerals of cumulate rocks, and the concentration of trace elements in the coexisting liquids. Chem. Geol., 118: 143-53

Bénard A., and. Ionov D.A., 2012. A new petrogenetic model for low-Ca boninites: Evidence from veined sub-arc xenoliths on melt-mantle interaction and melt fractionation, Geochem. Geophys. Geosyst., 13: Q0AF05, doi:10.1029/2012GC004145.

Berly T.J., Hermann J., Arculus R.J. and Lapierre H., 2006. Supra-subduction zone pyroxenites from San Jorge and Santa Isabel (Solomon Islands). J. Petrol. 47: 1531-1555.

Bodinier J.-L. and Godard M., 2003. Orogenic, ophiolitic and abyssal peridotites. In: R.W. Carlson (Ed.), The mantle and core. Treatise on Geochemistry, Vol. 2: 103-170, Elsevier, Oxford, UK.

Bodinier J.-L. and Godard M., 2014. Orogenic, ophiolitic and abyssal peridotites. In: H.D. Holland and K.K. Turekian (Eds.) Treatise on Geochemistry, Vol. 2: 103-167, 2nd Ed Elsevier Science, Oxford, UK.

Bodinier J.-L., Garrido C.J., Chanefo I., Bruguier O. and Gervilla F., 2008. Origin of pyroxenite-peridotite veined mantle by refertilization reactions: Evidence from the Ronda peridotite (Southern Spain). J. Petrol., 49: 999-1025, doi: 10.1093/petrology/egn014

Bodinier J.-L., Guiraud M., Fabries J., Dostal J. and Dupuy C., 1987. Petrogenesis of layered pyroxenites from the Lherz, Freychinede and Prades ultramafic bodies (Ariege, French Pyrenees). Geochim. Cosmochim. Acta, 51: 279-290.

Bodinier J. L., Vasseur G., Vernières J., Dupuy C. and Fabriès J., 1990. Mechanisms of mantle metasomatism: geochemical evidence from the Lherz orogenic peridotite. J. Petrol., 31: 597-628.

Borghini G. and Fumagalli P., 2018. Subsolidus phase relations in a mantle pyroxenite: an experimental study from 0.7 to 1.5 GPa. Eur. J. Miner., 30 (2): 333-348, doi: 10.1127/ejm/2018/0030-2735.

Borghini G., Fumagalli P. and Rampone E., 2010. The stability of plagioclase in the upper mantle: subsolidus experiments on fertile and depleted lherzolite. J. Petrol., 51: 229-254, doi: 10.1093/petrology/egp079.

Borghini G., Fumagalli P. and Rampone E., 2011. The geobarometric significance of plagioclase in mantle peridotites: A link between nature and experiments. Lithos, 126: 42-53, doi: 10.1016/j.lithos.2011.05.012.

Borghini G., Rampone E., Zanetti A., Class C., Cipriani A., Hofmann A.W. and Goldstein S.L., 2013. Meter-scale Nd isotopic heterogeneity in pyroxenite-bearing Ligurian peridotites encompasses global-scale upper mantle variability. Geology, 41: 1055-1058.

Borghini G., Rampone E., Zanetti A., Class C., Cipriani A., Hofmann A.W. and Goldstein S.L., 2016. Pyroxenite layers in the Northern Apennines' upper mantle (Italy). Generation by pyroxenite melting and melt infiltration. J. Petrol., 57: 625-653, doi: 10.1093/petrology/egv074.

Borghini G., Rampone E., Zanetti A., Class C., Fumagalli P. and Godard M., 2020. Ligurian pyroxenite-peridotite sequences (Italy) and the role of melt-rock reaction in creating enriched-MORB mantle sources. Chem. Geol., 532: 119252. https://doi.org/10.1016/j.chemgeo.2019.07.027.

Brey G.P. and Köhler T., 1990. Geothermobarometry in four phase lherzolites II. New thermobarometers, and practical assessment of existing thermobarometers. J. Petrol., 31:1353-1378.

Cluzel D., Ulrich M., Jourdan F., Meffre S., Paquette J.-L., Audeat M.-A., Secchiari A. and Maurizot P., 2016. Early Eocene clinoenstatite boninite and boninite-series dikes of the ophiolite of New Caledonia; a witness of slab-derived enrichment of the mantle wedge in a nascent volcanic arc. Lithos, 260: 429-442.

Dijkstra A.H., Barth M.G., Drury M.R., Mason P.R.D. and Vissers R.M.L., 2003. Diffuse porous melt flow and melt-rock reaction in the mantle lithosphere at the slow-spreading ridge: a structural petrology and LA-ICP-MS study of the Othris Peridotite Massif (Greece). Geochem. Geophys. Geosyst., 4: 1-24.

Downes H., 2007. Origin and significance of spinel and garnet pyroxenites in the shallow lithospheric mantle: Ultramafic massifs in orogenic belts in Western Europe and NW Africa. Lithos, 99: 1-24.

Eslami A., 2015. Mineralogy, geochemistry and genesis of chromite and platinum group minerals at Cheshmeh-Bid chromite deposit, Neyriz ophiolite. M.Sci. thesis, Tarbiat Modares Univ. (Iran), 353 pp.

Eslami A., Ghaderi M., Griffin W.L., Gain S., Grieco G. and González-Jiménez J.M., 2015. Magmatic and post-magmatic signatures of chromian spinels in podiform chromitites from the Cheshmeh-Bid chromitite deposit, Khajeh-Jamali ophiolitic massifs, Iran. Ofioliti, 40 (2): 91-106.

Fumagalli P., Borghini G., Rampone E. and Poli S., 2017. Experimental calibration of Forsterite-Anorthite-Ca-Tschermak-Enstatite (FACE) geobarometer for mantle peridotites. Contrib. Miner. Petrol., 172: 38, doi: 10.1007/s00410-017-1352-2

Garrido C.J. and Bodinier J.-L., 1999. Diversity of mafic rocks in the Ronda peridotite: evidence for pervasive melt-rock reaction during heating of subcontinental lithosphere by upwelling asthenosphere. J. Petrol., 40: 729-754.

Garrido C.J., Bodinier J.-L., Dhuime B., Bosch D., Chanefo I., Bruguier O., Hussain S.S., Dawood H. and Burg J.-P., 2007. Origin of the island arc Moho transition zone via melt-rock reaction and its implications for intracrustal differentiation of island arcs: Evidence from the Jijal complex (Kohistan complex, northern Pakistan). Geology, 35: 683-686.

Godard M., Jousselin D. and Bodinier J.-L. 2000. Relationships between geochemistry and structure beneath a palaeo-spreading centre: a study of the mantle section in the Oman ophiolite. Earth Planet. Sci. Lett., 180: 133-148.

Gonzaga R.G., Lowry D., Jacob D.E., LeRoex A., Schulze D. and Menzies M.A., 2010. Eclogites and garnet pyroxenites: similarities and differences. J. Volcanol. Geotherm Res., 190: 235-247.

Govindaraju K., 1994. 1994 compilation of working values and sample description for 383 geostandards. Geostand. Newsl., 18: 1-158.

Green D.H. and Falloon T.J., 1998. Pyrolite: a Ringwood concept and its current expression. In: I. Jackson (Ed.), The Earth's mantle. Cambridge Univ. Press, p. 311-378, doi: 10.1017/CBO9780511573101.010.

Grieco G., Bussolesi M., Tzamos E., Kapsiotis A. and Rassios A., 2018. Processes of primary and re-equilibration mineralization affecting chromitite ore geochemistry within the Vourinos ultramafic sequence, Vourinos Ophiolite (West Macedonia, Greece). Ore Geol. Rev., 95: 537-551.

Griffin W.L., Wass S.Y. and Hollis JD., 1984. Ultramafic xenoliths from Bullenmerri and Gnotuk Maars, Victoria, Australia: petrology of a sub-continental crust-mantle transition. J. Petrol., 25: 53-87.

Gysi A.P., Jagoutz O., Schmidt M.W. and Targuisti K., 2011. Petrogenesis of pyroxenites and melt infiltrations in the ultramafic complex of Beni Bousera, northern Morocco. J. Petrol., 52: 1679-1735.

Hart S.R. and Dunn T., 1993. Experimental cpx/melt partitioning of 24 trace elements. Contrib. Miner. Petrol., 113: 1-8.

Ionov D.A., Bodinier J.-L., Mukasa S.B. and Zanetti A., 2002. Mechanisms and sources of mantle metasomatism: Major and trace element compositions of peridotite xenoliths from Spitsbergen in the context of numerical modelling. J. Petrol., 43: 2219-2259.

Ionov D.A., Savoyant L. and Dupuy C., 1992. Application of the ICP-MS technique to trace element analysis of peridotites and their minerals. Geostand. Newsl., 16: 311-315.

Jochum K.P., Weis U., Schwager B., Stoll B., Wilson S.A., Haug G.H., Andreae M.O. and Enzweile J., 2016. Reference values following ISO guidelines for frequently requested rock reference materials. Geostand. Geoanalyt. Res., 40: 333-350.

Kamenetsky V.S., Sobolev A.V., Eggins S.M., Crawford A.J. and Arculus R.J., 2002. Olivine-enriched melt inclusions in chromites from low-Ca boninites, Cape Vogel, Papua New Guinea: Evidence for ultramafic primary magma, refractory mantle source and enriched components. Chem. Geol., 183: 287-303.

Kogiso T., Hirschmann M.M. and Reiners W., 2004. Length scales of mantle heterogeneities and their relationship to ocean island basalt geochemistry. Geochim. Cosmochim. Acta, 68: 345-360.

Kornprobst J., Piboule M., Roden M. and Tabit A., 1990. Corundum-bearing garnet clinopyroxenites at Beni Bousera (Morocco): original plagioclase-rich gabbros recrystallized at depth within the mantle? J. Petrol., 31: 717-745.

Kumar N., Reisberg L. and Zindler A., 1996. A major and trace element and strontium, neodymium, and osmium isotopic study of a thick pyroxenite layer from the Beni Bousera ultramafic complex of northern Morocco. Geochim. Cosmochim. Acta, 60: 1429-1444.

Lambart S., Baker M.B. and Stolper E.M., 2016. The role of pyroxenite in basalt genesis: Melt-PX, a melting parameterization for mantle pyroxenites between 0.9 and 5 GPa, J. Geophys. Res. Solid Earth.,121: 5708-5735, doi: 10.1002/2015JB012762.

Lambart S., Laporte D. and Schiano P., 2009. An experimental study of pyroxenite partial melts at 1 and 1.5 GPa: implications for the major-element composition of mid-ocean ridge basalts. Earth Planet. Sci. Lett., 288: 335-347.

Lambart S., Laporte D. and Schiano P., 2013. Markers of the pyroxenite contribution in the major element compositions of oceanic basalts: Review of the experimental constraints. Lithos, 160-161: 14-36.

Leake B., Woolley A., Arps C., Birch W., Gilbert M.C., Grice J.D., Hawthorne F.C., Kato A., Kisch H.J., Krivovichev V.G., Linthout K., Laird J., Mandarino J.A., Maresch W.V., Nickel E.H., Rock N.M.S., Schumacher J.C., Smith D.C., Ungaretti L., Whittaker E.J.W. and Youzhi G., 1997. Nomenclature of Amphiboles; Report of the Subcommittee on Amphiboles of the Intern. Miner. Ass. Commission on New Minerals and Mineral Names. Miner. Mag., 61: 295-310, doi: 10.1180/minmag.1997.061.405.13.

Le Roux V. and Liang Y., 2019. Ophiolitic pyroxenites record boninite percolation in subduction zone mantle. Minerals, 9: 565, doi: 10.3390/min9090565.

Marchesi C., Garrido C. J., Bosch D., Bodinier J.-L., Gervilla F. and Hidas K., 2013. Mantle refertilization by melts of crustal-derived garnet pyroxenite: Evidence from the Ronda peridotite massif, southern Spain. Earth Planet. Sci. Lett., 362: 66-75.

Marchesi C., Garrido C.J., Godard M., Belley F. and Ferré E., 2009. Migration and accumulation of ultra-depleted subduction-related melts in the Massif du Sud ophiolite (New Caledonia). Chem. Geol., 266 (3-4): 171-186.

Miura M. and Arai S., 2014. Platinum-group element and mineral characteristics of sub-arc chromitite xenoliths from the Takashima alkali basalt, southwest Japan Arc. Can. Miner., 52: 899-916.

Monsef I., Monsef R., Mata J., Zhang Z., Pirouz M., Rezaeian M., Esmaeili R. and Xiao W., 2018. Evidence for an early-MORB to fore-arc evolution within the Zagros suture zone: Constraints from zircon U-Pb geochronology and geochemistry of the Neyriz ophiolite (South Iran). Gondw. Res., 62: 287-305.

Montanini A. and Tribuzio R., 2015. Evolution of recycled crust within the mantle: constraints from the garnet pyroxenites of the External Ligurian ophiolites (Northern Apennines, Italy). Geology, 43: 911-914, doi: 10.1130/G36877.1

Montanini A., Tribuzio R. and Anczkiewicz R., 2006. Exhumation history of a garnet pyroxenite-bearing mantle section from a continent ocean transition (Northern Apennine ophiolites, Italy). J. Petrol., 47: 1943-1971, doi: 10.1093/petrology/egl032.

Montanini A., Tribuzio R. and Thirlwall M., 2012. Garnet clinopyroxenite layers from the mantle sequences of the Northern Apennine ophiolites (Italy): Evidence for recycling of crustal material. Earth Planet. Sci. Lett., 351-352: 171-181, doi: 10.1016/j.epsl.2012.07.033.

Morimoto N., 1988. Nomenclature of Pyroxenes. Miner. Petrol., 39: 55-76. https://doi.org/10.1007/BF01226262

Morishita T. and Arai S., 2001. Petrogenesis of corundum-bearing mafic rock in the Horoman Peridotite Complex, Japan. J. Petrol., 42: 1279-1299.

Mukasa S.B. and Shervais J.W., 1999. Growth of sub-continental lithosphere: evidence from repeated injections in the Balmuccia lherzolite massif, Italian Alps. Lithos, 48: 287-316.

Nandedkar R.H., Hürlimann N., Ulmer P. and Muntener O., 2016. Amphibole-melt trace element partitioning of fractionating calc-alkaline magmas in the lower crust: an experimental study. Contrib. Miner. Petrol., 171: 71. https://doi.org/10.1007/s00410-016-1278-0

Niida K. and Green D.H., 1999. Stability and chemical composition of pargasitic amphibole in MORB pyrolite under upper mantle conditions. Contrib. Miner. Petrol., 135: 18-40.

Niu Y.L., 1997. Mantle melting and melt extraction processes beneath ocean ridges: evidence from abyssal peridotites. J. Petrol., 38: 1047-1074.

O'Hara M.J., 1968. The bearing of phase equilibria studies insynthetic and natural systems on the origin and evolution of basic and ultrabasic rocks. Earth Sci. Rev., 4: 69-133.

Parkinson I.J. and Pearce J.A., 1998. Peridotites from the Izu-Bonin-Mariana fore-arc (ODP Leg125): evidence for mantle melting and melt-mantle interaction in a supra-subduction zone setting J. Petrol., 39: 1577-1618.

Pearson D.G., Davies G.R. and Nixon P.H., 1993. Geochemical constraints on the petrogenesis of diamond facies pyroxenites from the Beni Bousera peridotite massif, North Morocco. J. Petrol., 34: 125-172.

Piccardo G.B. and Vissers R.L.M., 2007. The pre-oceanic evolution of the Erro-Tobbio peridotite (Voltri Massif - Ligurian Alps, Italy). J. Geodyn., 43: 417-449.

Putirka K., 2016. Amphibole thermometers and barometers for igneous systems and some implications for eruption mechanisms of felsic magmas at arc volcanoes. Am. Miner., 101: 841-858, doi: https://doi.org/10.2138/am-2016-5506.

Python M. and Ceuleneer G., 2003. Nature and distribution of dykes and related melt migration structures in the mantle section of the Oman ophiolite. Geochem. Geophys. Geosyst., 4, doi: 10.1029/2002GC000354.

Rajabzadeh M.A., 1998. Minéralisation en chromite et éléments du groupe du platine dans les ophiolites d'Assemion et de Neyriz, centre du Zagros, Iran. Ph.D. Thesis, Inst. Nat. Polytechn. Lorraine, France, 358 pp.

Rajabzadeh M.A. and Moosavinasab Z., 2012. Mineralogy and distribution of platinum-group minerals (PGM) and other solid inclusions in the Neyriz ophiolitic chromitite, southern Iran. Can. Miner., 50: 643-665.

Rajabzadeh M.A. and Nazari-Dehkordi T., 2013. Investigation on mantle peridotites from Neyriz ophiolite, south of Iran: geodynamic signals. Arab. J. Geosci., 6: 4445-4461.

Rajabzadeh M.A., Nazari-Dehkordi T. and Caran S., 2013. Mineralogy, geochemistry and geotectonic significance of mantle peridotites with high-Cr chromitites in the Neyriz ophiolite from the outer Zagros ophiolite belts, Iran. J. Afr. Earth. Sci., 78: 1-15.

Rampone E. and Borghini G., 2008. The melt intrusion/interaction history of the Erro-Tobbio peridotites (Ligurian Alps, Italy): insights on mantle processes at non-volcanic passive margins. Eur. J. Miner., 20: 573-585.

Rampone E., Borghini G. and Basch V., 2020. Melt migration and melt-rock reaction in the Alpine-Apennine peridotites: Insights on mantle dynamics in extending lithosphere. Geosci. Front., 1: 151-166.

Rampone E., Piccardo G.B. and Hofmann A.W., 2008. Multi-stage melt-rock interaction in the Mt. Maggiore (Corsica, France) ophiolitic peridotites: microstructural and geochemical evidence. Contrib. Miner. Petrol., 156: 453-475.

Rogkala A., Petrounias P., Tsikouras B. and Hatzipanagiotou K., 2017. New occurrence of pyroxenites in the Veria-Naousa ophiolite (North Greece): implications on their origin and petrogenetic evolution. Geosciences, 7: 92; doi:10.3390/geosciences7040092

Saccani E., Beccaluva L., Photiades A. and Zeda O., 2011. Petrogenesis and tectonomagmatic significance of basalts and mantle peridotites from the Albanian-Greek ophiolites and sub-ophiolitic mélanges. New constraints for the Triassic-Jurassic evolution of the Neo-Tethys in the Dinaride sector. Lithos, 124: 227-242.

Secchiari A., Montanini A., Bosch D., Macera P. and Cluzel D., 2020. Sr, Nd, Pb and trace element systematics of the New Caledonia harzburgites: Tracking source depletion and contamination processes in a SSZ setting. Geosci. Front., 1: 37-55.

Seyler M., Lorand J.-P., Dick H.J.B. and Drouin M., 2007. Pervasive melt percolation reactions in ultra-depleted refractory harzburgites at the Mid-Atlantic Ridge, 15° 20'N: ODP Hole 1274A. Contrib. Miner. Petrol., 153: 303-319.

Shafaii Moghadam H. and Stern R.J., 2015. Ophiolites of Iran: Keys to understanding the tectonic evolution of SW Asia: (II) Mesozoic ophiolites. J. Asian Earth Sci., 100: 31-59.

Shafaii Moghadam H., Zaki Khedr M., Chiaradia M., Stern R.J., Bakhshizad F., Arai S., Ottley C.J., and Tamura A., 2014. Supra-subduction zone magmatism of the Neyriz ophiolite, Iran: constraints from geochemistry and Sr-Nd-Pb isotopes. Intern. Geol. Rev., 56: 1395-1412, doi: 10.1080/00206814.2014.942391

Shervais J.W. and Jean M.M., 2012. Inside the subduction factory: modeling fluid-mobile element enrichment in the mantle wedge above a subduction zone. Geochim. Cosmochim. Acta, 95: 270-285.

Sun S.S. and McDonough W.F., 1989. Chemical and isotopic systematics of ocean basalts: Implications for mantle composition-and processes. In: A.D. Saunders and M.J. Norry (Eds.), Magmatism in the ocean basins. Geol. Soc. London Spec. Publ., 42: 313-346.

Taghipour B. and Ahmadnejad F., 2018. Platinum-group elements geochemistry and chromian spinel composition in podiform chromitites and associated peridotites from the Cheshmeh-Bid deposit, Neyriz, Southern Iran: implications for geotectonic setting. Acta Geol. Sin., 92: 183-209.

Takazawa E., Frey F.A., Shimizu N., Saal N. and Obata M., 1999. Polybaric petrogenesis of mafic layers in the Horoman peridotite complex, Japan. J. Petrol., 40: 1827-1831.

Tamura A. and Arai S., 2006. Harzburgite-dunite-orthopyroxenite suite as a record of supra-subduction zone setting for the Oman ophiolite mantle. Lithos, 90: 43-56.

Taylor R.N., Nesbitt R.V., Vidal P., Russel S., Harmon R.S., Auvray B. and Croudace I.W. 1994. Mineralogy, chemistry, and genesis of the boninite series volcanics, Chichijima, Bonin Islands, Japan. J. Petrol., 35: 577-617.

Tilhac R., Ceuleneer G., Griffin W.L., O'Reilly S.Y., Pearson N.J., Benoit M., Henry H., Girardeau J. and Grégoire M., 2016. Primitive arc magmatism and delamination: petrology and geochemistry of pyroxenites from the Cabo Ortegal Complex, Spain, J. Petrol., 57: 1921-1954. https://doi.org/10.1093/petrology/egw064.

Varfalvy V., Hébert R., Bédard J. and Laflèche M.R., 1997. Petrology and geochemistry of pyroxenite dykes in upper mantle peridotites of the North Arm Mountain massif, Bay of Islands Ophiolite, Newfoundland: Implications for the genesis of boninitic and related magmas. Can. Miner., 35: 543-570.

Zanetti A., D'Antonio M., Spadea P., Raffone N., Vannucci R. and Bruguier O., 2006. Petrogenesis of mantle peridotites from the Izu-Bonin-Mariana (IBM) forearc. Ofioliti, 31: 189-206.

Received, December 4, 2020
Accepted, January 7, 2021